
Animate Your Thoughts: Decoupled Reconstruction of Dynamic Natural Vision from Slow Brain Activity

Yizhuo Lu^{1,2,3*}, Changde Du^{1,2*}, Chong Wang⁴, Xuanliu Zhu⁵, Liyun Jiang^{1,2,3},
Huiguang He^{1,2,3†}

¹Key Laboratory of Brain Cognition and Brain-inspired Intelligence Technology

²State Key Laboratory of Multimodal Artificial Intelligence Systems, CASIA, Beijing, China

³School of Future Technology, University of Chinese Academy of Sciences

⁴School of Computer and Artificial Intelligence, Zhengzhou University, Zhengzhou, China

⁵Beijing University of Posts and Telecommunications, Beijing, China

luyizhuo2023@ia.ac.cn, changde.du@ia.ac.cn, huiguang.he@ia.ac.cn,
vincenzo@zzu.edu.cn, 1293098990@bupt.edu.cn

Abstract

Reconstructing human dynamic vision from brain activity is a challenging task with great scientific significance. The difficulty stems from two primary issues: (1) vision-processing mechanisms in the brain are highly intricate and not fully revealed, making it challenging to directly learn a mapping between fMRI and video; (2) the temporal resolution of fMRI is significantly lower than that of natural videos. To overcome these issues, this paper propose a two-stage model named Mind-Animator, which achieves state-of-the-art performance on three public datasets. Specifically, during the fMRI-to-feature stage, we decouple semantic, structural, and motion features from fMRI through fMRI-vision-language tri-modal contrastive learning and sparse causal attention. In the feature-to-video stage, these features are merged to videos by an inflated Stable Diffusion. We substantiate that the reconstructed video dynamics are indeed derived from fMRI, rather than hallucinations of the generative model, through permutation tests. Additionally, the visualization of voxel-wise and ROI-wise importance maps confirms the neurobiological interpretability of our model.

1 Introduction

Researchers in computational neuroscience and the field of artificial intelligence have long sought to decipher and simulate the brain’s visual information processing mechanisms to advance the development of brain-inspired models [1–3].

In recent years, functional magnetic resonance imaging (fMRI) has emerged as a reliable tool for measuring brain activity due to its high spatial resolution as a non-invasive brain signal recording technique [4]. fMRI-based neural decoders, which map brain signals to visual stimuli, facilitate a deeper understanding of the human visual perception system. Neural decoding can be categorized into classification, identification, and reconstruction, with this study focusing on the most challenging aspect: reconstruction. Prior research has made significant strides in the classification [3, 5–8] and identification [4, 9–11] of **static** stimulus images, and remarkably, some researchers have advanced to the point where they can reconstruct [12–22] images from brain signals that closely resemble the original stimulus images.

*Equal contributions

†Huiguang He is the corresponding author.

In reality, the majority of visual stimuli we encounter in daily life are **continuous** and **dynamic**. As depicted in Figure 1, when a subject views dynamic scenes, the primary visual cortex firstly processes low-level structural information like location, shape, size, and color [23], leading to the preliminary recognition of a black silhouette at the edge of a yellow background. Subsequently, motion information of the object is perceived [24], noting that the silhouette is moving from right to left. Lastly, in the higher visual cortex, the interpretation of category and description gives rise to high-level semantic understanding [25], comprehending the scene as a soldier walking from right to left in a desert.

Due to the inherent nature of fMRI, which relies on the slow blood oxygenation level dependent (BOLD) [26, 27] signal, the sampling frequency is restricted to around 0.5Hz. This frequency is notably lower than the typical 30Hz frame rate of most videos. As a result, a significant discrepancy exists between the temporal resolution of fMRI and the nature video. In fact, each fMRI signal integrates information from approximately 60 video frames. This disparity makes the task of **reconstructing video from fMRI signals** an exceedingly complex challenge.

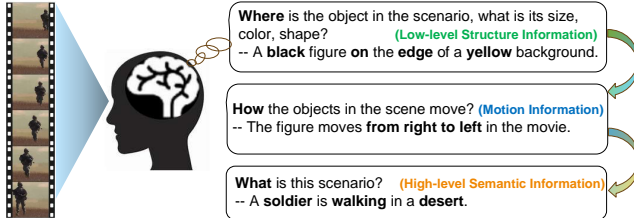


Figure 1: **The human brain’s comprehension of dynamic visual scenes.** When receiving dynamic visual information, human brain gradually comprehends *low-level structural* details such as position, shape and color in the primary visual cortex, discerns *motion* information, and ultimately constructs *high-level semantic* information in the higher visual cortex, such as an overall description of the scene.

To address this challenge, Nishimoto [28] transforms the video reconstruction task into a identification problem, employing the Motion-Energy model [29] and Bayesian inference to reconstruct videos from a predefined video library. Subsequently, Han [30] and Wen [31] et al. map brain responses to the feature spaces of deep neural network (DNN) to reconstruct down-sampled (with the frame rate reduced to 1Hz) video stimuli. Wang [32] et al. develop an f-CVGAN that learns temporal and spatial information in fMRI through separate discriminators [33]. To mitigate the scarcity of video-fMRI data, Kupersmidt [34] et al. utilize self-supervised learning [35] to incorporate a large amount of unpaired video data. These efforts have validated the feasibility of video reconstruction from fMRI, albeit with a lack of explicit semantic information in the results. Chen [36] et al. utilize contrastive learning to map fMRI to the Contrastive Language-Image Pre-Training (CLIP) [37] representation space and fine-tuned inflated Stable Diffusion [38, 39] on a video-text dataset as a video generation model, successfully reconstructing coherent videos with clear semantic information for the first time. However, this work does not consider structure information such as color and position, and it is uncertain whether the motion information in the reconstructed videos originated from the fMRI or the video generation model.

Method	Semantic	Structure	Motion	Frame rate	Resolution
Nishimoto [28] (Current Biology 2011)	×	×	✓	—	—
Wen [31] (Cerebral Cortex 2017)	×	✓	×	—	64x64
Han [30] (NeuroImage 2019)	×	✓	×	—	128x128
Kupersmidt [34]	×	✓	(✓)	4Hz	112x112
Wang [32] (Cerebral Cortex 2022)	×	✓	✓	4Hz	64x64
Chen [36] (NeurIPS 2023 Oral)	✓	×	(✓)	3Hz	256x256
Ours	✓	✓	✓	4Hz	512x512

Table 1: Comparison of modal information used in Mind-Animator and related works. Parentheses indicate the utilization of external video data in the decoding of this feature.

In summary, current video reconstruction models face two challenges:

- (1) As shown in Table 1, they fail to simultaneously capture semantic, structure, and motion information within the reconstructed videos. Moreover, the resolution of the video is low.

- (2) The reliance on external video datasets and video generation models introduces uncertainty regarding the true source of motion information, leading to the possibility that the reconstructed videos may represent a "hallucination" of the video generation model rather than an accurate dynamic decoding from the fMRI data.

To address the aforementioned issues, we introduce Mind-Animator, a video reconstruction model that decouples semantic, structure, and motion information from fMRI, as illustrated in Figure 2. Specifically, we map fMRI to the CLIP representation space and the Vector Quantized-Variational Autoencoder (VQ-VAE) [40] latent space to capture semantic and structure information. We design a Transformer-based [41] motion decoder to extract motion information frame by frame from fMRI through a next-frame-prediction task. Finally, the decoded semantic, structure, and motion information is fed into an inflated Stable Diffusion [38, 39] **without any fine-tuning** to generate each frame of the video, ensuring that all information is derived solely from the fMRI data.

The contributions are summarized as follows:

- (1) We propose Mind-Animator, which for the first time successfully decouples semantic, structure, and motion information from fMRI to enable video reconstruction. To extract the motion and spatial information from fMRI, we propose temporal and spatial attention modules respectively, which decode subtle but significant motion information.
- (2) We validate through a permutation test that the motion information in our reconstructed videos indeed originates from the fMRI, rather than being a "hallucination" generated by the video generation model.
- (3) We introduce **seven** evaluation metrics that comprehensively assess the reconstruction results of our model and all previous models across three dimensions—semantic, structure, and spatiotemporal consistency—on **three** publicly available high-quality video-fMRI datasets. Our model achieves state-of-the-art (SOTA) performance in five of these metrics and secures second place in the remaining two, with a notable 76% improvement in Structural Similarity Index (SSIM) over the previous SOTA. This establishes our work as the first comprehensive and unbiased benchmark for subsequent researchers. The code and data have been anonymously released at: <https://github.com/Zuskd/Mind-Animator>.

2 Methodology

2.1 Overview

Figure 2 presents the overall architecture of the proposed Mind-Animator, a video reconstruction model based on fMRI. The model consists of two stages: fMRI-to-feature and feature-to-video.

In the fMRI-to-feature stage, as depicted in Figure 1, we begin by emulating the human visual system’s approach to interpreting dynamic visual stimuli. This process involves the decomposition of video stimuli into high-level semantic feature, low-level structural feature, and motion feature. Then three separate decoders are trained to decode these features from fMRI: **(a)** for decoding semantic feature, we employ a contrastive learning loss to map fMRI into the visual-linguistic embedding space of CLIP[37], **(b)** we utilize the frame token extracted by VQ-VAE[40] as the video’s structural feature[42], followed by a simple Multi-Layer Perceptron (MLP) to fit it, and **(c)** we design a Transformer-based Consistency Motion Generator for decoding motion information. After training with a next-frame-prediction task, this module sequentially generates each subsequent frame token based on the first frame token decoded in section (b).

In the feature-to-video stage, depicted in Figure 2 (d), the decoded features are input into an inflated Text-to-Image (T2I) model, facilitating the reconstruction of the stimulus video without the interference of external training videos.

2.2 Problem Statement

We aim to decode videos from brain activity recorded with fMRI when healthy participants watch a sequence of natural videos. Let X and Y denote the voxel space and pixel space, respectively. Let $X_i \in R^{1 \times n}$ be the fMRI signal when a video $V_{i,j} \in R^{1 \times 3 \times 512 \times 512}$ is presented to the participant, where n is the number of fMRI voxels, j is the frame ID of video i and $i \in [1, N]$, $j \in [1, 8]$, with N

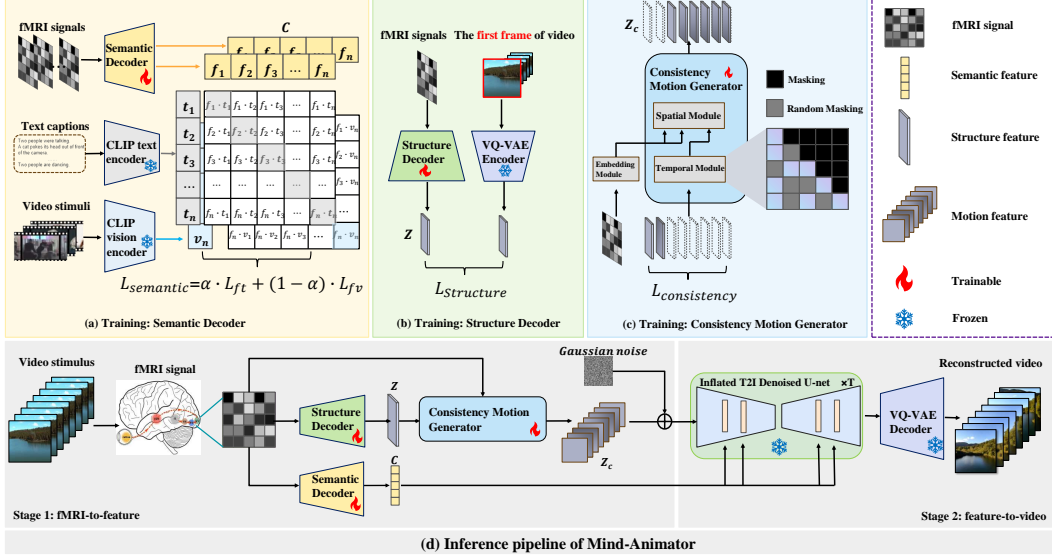


Figure 2: The overall architecture of Mind-Animator, a two-stage video reconstruction model based on fMRI. As illustrated in subfigures (a), (b), and (c), three decoders are trained during the **fMRI-to-feature** stage to disentangle semantic, structural, and motion information from fMRI, respectively. Subfigure (d) demonstrates that, in the **feature-to-video** stage, the decoded information is input into an inflated Text-to-Image (T2I) model for video reconstruction.

the total number of videos. Let $Z(k)$ denote the feature space, $k \in \{semantic, structure, motion\}$. The goal of fMRI-to-feature stage is to train decoders $D(k) : X \rightarrow Z(k)$, and the goal of feature-to-video stage is to construct a video generation model $G : Z(semantic) \times Z(structure) \times Z(motion) \rightarrow Y$, without introducing motion information from external video data.

2.3 fMRI-to-feature Stage

Semantic Decoder Due to the low signal-to-noise ratio of the fMRI signal X_i and the substantial dimension discrepancy with the text condition $c_i \in R^{1 \times 20 \times 768}$, directly learning a mapping between them is prone to overfitting. Considering the robust semantic information embedded in the latent space of CLIP[43], and given that CLIP has been shown to outperform various single-modal DNNs in explaining cortical activity[44, 45], we employ bidirectional InfoNCE loss to align the fMRI with the latent space of CLIP (Vit-B/32) $\in R^{512}$, followed by a two-layer MLP to map it to text condition c_i ,

$$L_{BiInfoNCE} = -\frac{1}{B} \sum_{i=1}^B \left(\log \frac{\exp(s(\hat{z}_i, z_i)/\tau)}{\sum_{j=1}^B \exp(s(\hat{z}_i, z_j)/\tau)} + \log \frac{\exp(s(\hat{z}_i, z_i)/\tau)}{\sum_{k=1}^B \exp(s(\hat{z}_i, z_k)/\tau)} \right). \quad (1)$$

where s is the cosine similarity, z_i and \hat{z}_i are the latent representation from two modalities, B is the batch size, and τ is a learned temperature parameter. Then, given $f \in R^{B \times 512}$, $v \in R^{B \times 512}$, and $t \in R^{B \times 512}$ as the respective representations of fMRI, video, and text embeddings, the fMRI-vision-language trimodal loss is:

$$L_{Semantic} = \alpha \cdot L_{BiInfoNCE}(f, t) + (1 - \alpha) \cdot L_{BiInfoNCE}(f, v). \quad (2)$$

Subsequently, to map the fMRI embedding f_i to the text condition c_i for the purpose of conditioning generative image models, a projection loss is utilized,

$$L_{Projection} = \frac{1}{B} \sum_{i=1}^B \|MLP(f_i) - c_i\|_2^2. \quad (3)$$

Finally, we combine the Semantic and Projection losses using tuned hyperparameters λ_1, λ_2 ,

$$L_{Combined} = \lambda_1 \cdot L_{Semantic} + \lambda_2 \cdot L_{Projection}. \quad (4)$$

Structure Decoder For a short video clip, it can be assumed that the low-level information (size, shape, and color) contained in each frame remains largely consistent with that of the first frame. Consequently, we utilize the token extracted from the first frame by VQ-VAE as structural information and train the structural decoder using the standard mean squared error (MSE) loss function. Let Φ denote the encoder of VQVAE, the structure loss is defined as:

$$L_{Structure} = \frac{1}{B} \sum_{i=1}^B \|D_{Structure}(f_i) - \Phi(V_{i,1})\|_2^2. \quad (5)$$

Consistency Motion Generator Inspired by natural language processing, we treat each video frame token as a word embedding, and develop an L-layer Transformer-based Consistency Motion Generator. For a more detailed introduction, please refer to Appendix B.1.

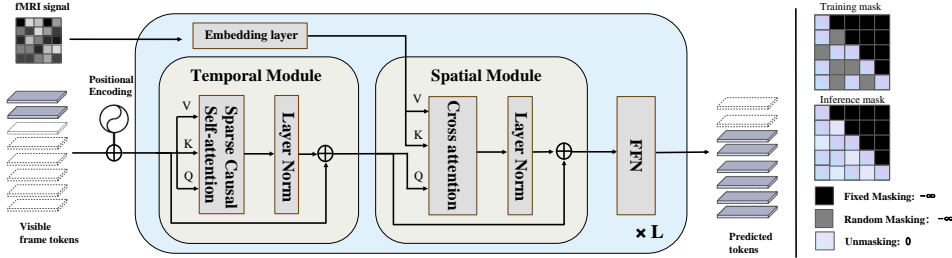


Figure 3: The detailed architectural diagram of the Consistency Motion Generator.

In the Temporal Module, visible video frame tokens $\Phi(V_i) \in R^{m \times d_{token}}$ and positional encoding $E_{pos} \in R^{m \times d_{token}}$ are jointly input into a Sparse Causal Self-Attention (SCSA) layer to learn inter-frame temporal information. This attention layer incorporates a specially designed Sparse Causal Mask to ensure sparsity between frames and accelerate training. As illustrated in Figure 3, the mask is divided into **fixed** and **random** components. The fixed mask ensures that each frame cannot access information from subsequent frames, while the random mask maintains sparsity among visible frames, preventing the model from taking shortcuts[52]. During inference, we eliminate the random mask. As shown in Eq. 6, the model also applies residual connections and layer normalization (LN) to the variable z_l ,

$$\begin{aligned} z_0 &= [\Phi(V_{i,1}), \Phi(V_{i,2}), \dots, \Phi(V_{i,m})] + E_{pos}, \\ z_l &= LN(SCSA(z_{l-1})) + z_{l-1}. \quad l = 1, 2, \dots, L \end{aligned} \quad (6)$$

As shown in Eq. 7, in the Spatial Module, the embedding of the visible frames z_l serves as the Query, while the fMRI signal f , after passing through an embedding layer, serves as the Key and Value in the cross-attention block. Following residual connections and layer normalization, z_l is input into the Feed Forward Network (FFN) to predict the subsequent unseen frame tokens $\Phi(\hat{V}_{i,j}), j \in [m+1, 8]$:

$$z_l = CrossAttention(Q, K, V), \quad l = 1, 2, \dots, L \quad (7)$$

$$\begin{aligned} Q &= W_Q^l \cdot z_l, \quad K = W_K^l \cdot Emb(f), \quad V = W_V^l \cdot Emb(f), \\ z_l &= FFN(LN(z_l) + z_{l-1}). \quad l = 1, 2, \dots, L \end{aligned} \quad (8)$$

Then, the final motion consistency loss is defined as:

$$L_{Consistency} = \frac{1}{B} \sum_{i=1}^B \sum_{j=m+1}^8 \|\Phi(\hat{V}_{i,j}) - \Phi(V_{i,j})\|_2^2. \quad (9)$$

2.4 Feature-to-video Stage

Inflated Stable Diffusion for Video Reconstruction Despite the rapid development of video generation models capable of producing vivid videos from text conditions, it is crucial to emphasize that the objective of our project is to disentangle semantic, structural, and motion information from

fMRI to fully reconstruct the stimulus video. Utilizing pre-trained video generation models could obscure whether the motion information in the reconstructed video originates from the fMRI or external video data.

To address this issue, we employ the network inflation[39, 46, 47] technique to implement an inflated Stable Diffusion, which is used to reconstruct each frame of the video without introducing additional motion information. For further details, please refer to the Appendix B.2.

3 Experiment

3.1 Datasets

In this study, we utilize three publicly available video-fMRI datasets, which encompass paired stimulus videos and their corresponding fMRI responses. As depicted in Table 2, these datasets collectively comprise brain signals recorded from multiple healthy subjects while they are viewing the videos. The video stimuli are diverse, covering animals, humans, and natural scenery. For detailed information on the datasets and preprocessing steps, please refer to Appendix C.

Dataset	Adopted participants	TR	Train samples	Test samples
CC2017[31]	3	2s	4320	1200
HCP[48]	3	1s	2736	304
Algonauts2021[49]	10	1.75s	900	100

Table 2: Characteristics of the video-fMRI datasets used in our experiments

3.2 Evaluation Metrics

To comprehensively and fairly evaluate the performance of our model, we propose the following evaluation metrics.

Semantic-level metrics Following prior studies[19, 36], we use the N-way top-K accuracy classification test and VIFI-score as the semantics-level metrics. For the classification test, we compare the ground truth (GT) against the predicted video (PV) classifications using a classifier. A trial is successful if the GT class ranks within the top-K probabilities from the PV’s classification among N randomly selected classes. Additionally, we implement two modes: image-based (2-way-I) and video-based (2-way-V). We describe this evaluation method in Algorithm 2. For the VIFI-score, we utilize VIFICLIP[53]—a CLIP model fine-tuned on the video dataset—to extract features from both the GT and the PV, followed by the calculation of cosine similarity.

Pixel-level metrics We employ the structural similarity index measure (SSIM), peak signal-to-noise ratio (PSNR), and hue-based Pearson correlation coefficient (Hue-pcc) as pixel-level metrics.

Spaciotemporal (ST) -level metric We adopt the CLIP-pcc, a common metric in the field of video editing, which involves computing CLIP image embeddings on each frame of the predicted videos and reporting the average cosine similarity between all pairs of adjacent video frames.

4 Results

4.1 Comparative Experimental Results

We compare our model with all previous video reconstruction models³ on the **CC2017** dataset. Visual comparisons are presented in Figure 4, while quantitative comparisons are detailed in Table 3. In the computation of quantitative metrics, the results of Wen et al.[31] pertain to the first segment of the test set, whereas the results of other researchers are derived from the whole test set. The findings on **HCP** and **Algonauts2021** datasets are elaborated in Appendices E.2 and E.3, respectively.

³It should be noted that when replicating the results of Nishimoto et al.[28] on the CC2017 dataset, we utilized videos from the training sets of both CC2017 and HCP as the natural movie prior.

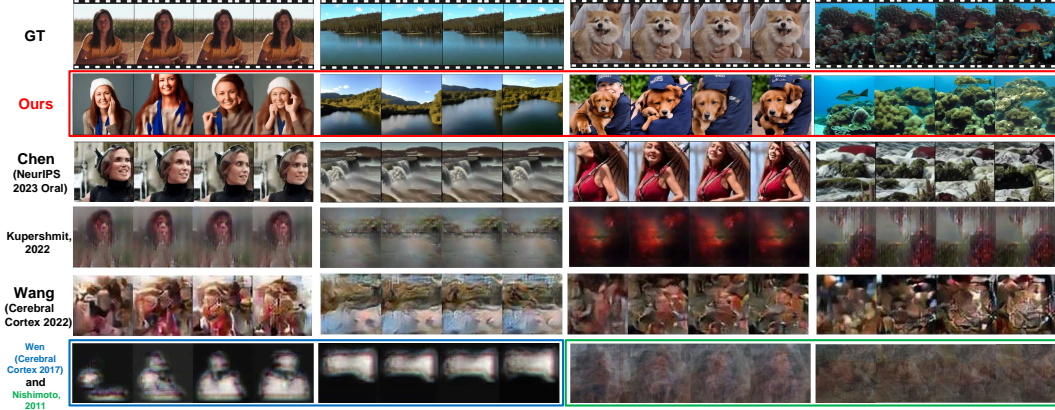


Figure 4: Reconstruction results of CC2017 dataset. Our reconstructed results are highlighted with red boxes, while those of Wen and Nishimoto are delineated by blue and green boxes, respectively.

	Semantic-level \uparrow			Pixel-level \uparrow			ST-level \uparrow
	2-way-I	2-way-V	VIFI-score	SSIM	PSNR	Hue-pcc	CLIP-pcc
Nishimoto[28]	0.727 \pm 0.04	—	—	0.116 \pm 0.09	8.012 \pm 2.31	0.753 \pm 0.12	—
Wen[31]	0.758 \pm 0.03	—	—	0.114 \pm 0.15	7.646 \pm 3.48	0.647 \pm 0.11	—
Wang[32]	0.713 \pm 0.04	0.773 \pm 0.03	<u>0.596\pm0.07</u>	0.118 \pm 0.08	11.432\pm2.42	0.589 \pm 0.18	0.402 \pm 0.41
Kupershmidt[34]	0.764 \pm 0.03	0.771 \pm 0.03	0.585 \pm 0.08	0.135 \pm 0.08	8.761 \pm 2.22	0.606 \pm 0.14	0.386 \pm 0.47
Chen[36]	0.792 \pm 0.03	0.853\pm0.03	0.587 \pm 0.08	<u>0.171\pm0.08</u>	8.662 \pm 1.52	<u>0.760\pm0.10</u>	<u>0.408\pm0.46</u>
Ours(sub1)	0.809\pm0.03	<u>0.837\pm0.02</u>	0.602\pm0.07	0.301\pm0.09	<u>9.134\pm1.48</u>	0.768\pm0.12	0.425\pm0.42
Ours(sub2)	0.804 \pm 0.29	0.832 \pm 0.03	0.604 \pm 0.08	0.287 \pm 0.11	9.049 \pm 1.45	0.795 \pm 0.12	0.426 \pm 0.42
Ours(sub3)	0.792 \pm 0.03	0.833 \pm 0.03	0.600 \pm 0.08	0.349 \pm 0.11	9.306 \pm 1.54	0.791 \pm 0.12	0.415 \pm 0.39

Table 3: Quantitative comparison of reconstruction results. All metrics indicate superior performance with larger values, with the best results highlighted in bold and the second-best results underlined.

Table 3 indicates that our model achieves SOTA performance in 5 out of 7 metrics, securing the second place in the remaining two. Specifically, our model outperforms the previous SOTA model by 76% in terms of SSIM, which underscores the benefits of incorporating structural information. Specifically, as depicted in Figure 4, our reconstruction results contain richer semantic information compared to earlier models, such as a girl and a yellow dog being held in someone’s arms. In contrast to Mind-video by Chen et al.[36], our results are more consistent with the ground truth in terms of fine-grained structural and motion information. For instance, the reconstructed girl’s clothing color, the dog’s fur color, and the positioning of the forest along the coastline are closer to the stimulus videos. Regarding motion information, our results depict the dog being petted and a noticeable camera movement in the coral reef scene. Additional reconstruction results on other subjects, as well as instances of reconstruction failure, are presented in Appendix E.1.

4.2 Ablation Study

In this subsection, we conduct a detailed ablation study to assess the effectiveness of the three decoders we proposed and to evaluate the impact of various hyperparameters on video reconstruction (See Appendix E.4).

First, we present the results obtained using the full model. Then, on the basis of the full model, we separately eliminate the semantic decoder (w/o Semantic) and the structure decoder (w/o Structure) by replacing their outputs with random noise. For the consistency motion generator, we replaced it with 8 simple MLPs to model each frame individually (w/o Motion). Table 4 demonstrates that the removal of any decoder results in a significant decline in the model’s performance across nearly all metrics, which shows the efficacy of our proposed decoders.

	Semantic-level \uparrow			Pixel-level \uparrow			ST-level \uparrow
	2-way-I	2-way-V	VIFI-score	SSIM	PSNR	Hue-pcc	CLIP-pcc
w/o Semantic	0.679 \pm 0.04	0.766 \pm 0.04	0.523 \pm 0.07	0.097 \pm 0.09	8.005 \pm 1.57	0.737 \pm 0.11	0.123 \pm 0.31
w/o Structure	0.789 \pm 0.03	0.814 \pm 0.03	0.555 \pm 0.08	0.184 \pm 0.08	8.712 \pm 1.37	0.791 \pm 0.11	0.260 \pm 0.41
w/o Motion	0.674 \pm 0.04	0.789 \pm 0.03	0.585 \pm 0.08	0.136 \pm 0.13	8.611 \pm 2.43	0.715 \pm 0.14	0.376 \pm 0.42
Full Model	0.809 \pm 0.03	0.837 \pm 0.02	0.602 \pm 0.07	0.301 \pm 0.10	9.134 \pm 1.51	0.768 \pm 0.11	0.425 \pm 0.41

Table 4: **Ablation study** on our proposed decoders. 100 repetitions are conducted on the metrics 2-way-I and 2-way-V, while 5 trials are performed on other metrics, with the results being averaged across all samples in test set and trials. Colors reflect statistical significance (paired t-test) compared to the Full Model. $p < 0.0001$ (purple); $p < 0.01$ (pink); $p < 0.05$ (yellow); $p > 0.05$ (green).

5 Interpretability Analysis

5.1 Have we truly decoded motion information from fMRI?

This work focuses on the video reconstruction from fMRI, aiming for motion consistency between the reconstructed and stimulus videos. We specifically design a Consistency Motion Generator (CMG) to decode motion information from fMRI. Following the work of Wang et al. [32], we perform a permutation test on 3 subjects from the CC2017 dataset to ascertain whether this module decodes the correct motion information from fMRI. Specifically, for each 8-frame reconstructed video clip from each subject, we randomly shuffle the frame order 100 times and compute pixel-level and spatiotemporal-level metrics between the actual and shuffled frames. Subsequently, we estimate the P-value by the following formula: $P = \sum_{i=1}^{100} \delta_i / 100$, where $\delta_i = 1$ if the i th permutation outperforms the reconstruction result in the original order based on the metrics; otherwise, $\delta_i = 0$. A lower P-value signifies a closer alignment between the sequential order of the reconstructed video and the ground truth. We repeat the permutation test 5 times under conditions with and without the CMG, as illustrated in Figure 5. It can be observed that the P-value significantly increased across nearly all metrics for all subjects when the CMG is removed, suggesting that we truly decodes motion information from fMRI.

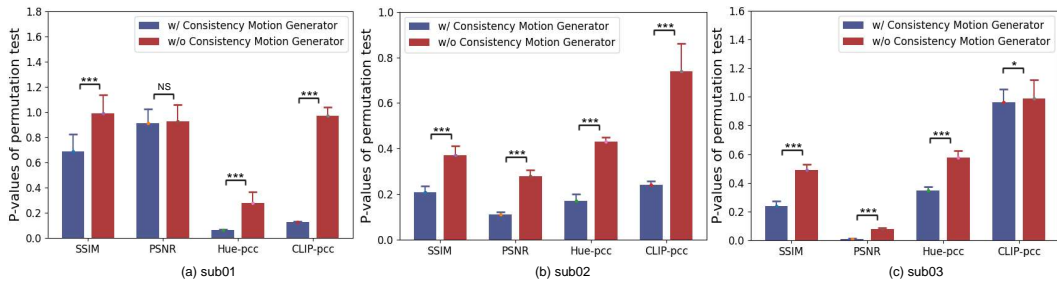


Figure 5: The result of permutation test on the CC2017 dataset. The experiment is repeated 5 times on 3 subjects, with the mean and std presented in subplots (a), (b), and (c), respectively. Paired t-tests are performed, with significance denoted as $p < 0.001$ (***), $p < 0.01$ (**), $p < 0.05$ (*), and $p > 0.05$ (NS) for non-significant results.

5.2 Which brain regions are responsible for decoding different features, respectively?

To investigate voxels in which brain regions are responsible for decoding different features (semantic, structure, motion) during the fMRI-to-feature stage, we compute the **voxel-wise** importance maps in the visual cortex. Specifically, for a trained decoder, we multiply the weight matrix of the linear layers, then average the result across the feature dimension, and normalize it to estimate the importance weight for each voxel. A higher weight indicates that the voxel plays a more significant role in feature decoding. We project the importance maps of subject 1’s voxels from the CC2017 dataset onto the visual cortex, as depicted in Figure 6. To obtain **ROI-wise** importance maps, we calculate the average of the importance weights of voxels contained within each Region of Interest (ROI), with the results presented in Figure 7. The results from other subjects are presented in Appendix E.5.

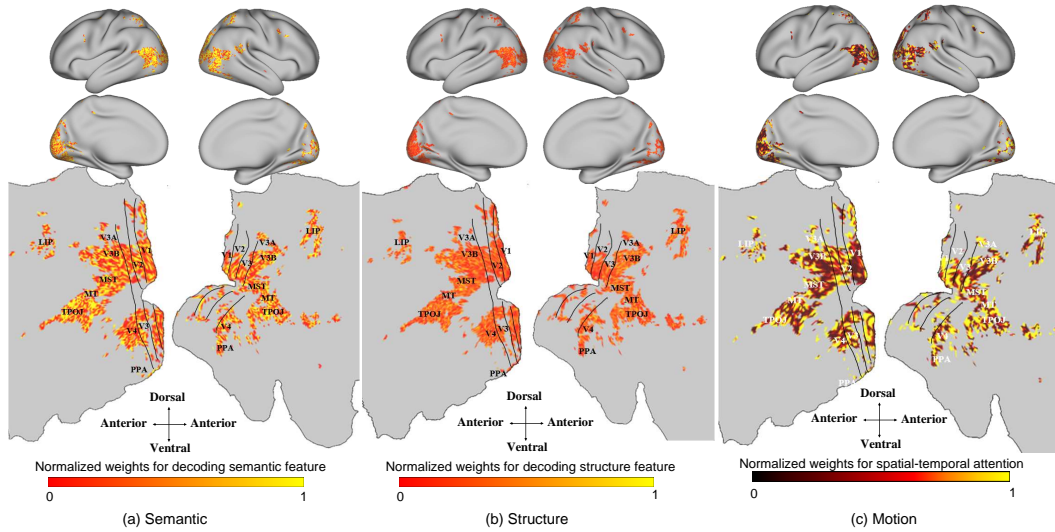


Figure 6: **Voxel-wise** importance maps projected onto the visual cortex of subject 1. The lighter the color, the greater the weight of the voxel in the interpretation of feature.

Figure 6 (a) indicates that high-level visual cortex (HVC, such as MT, MST and TPOJ) contribute more significantly to the decoding of semantic feature, with a calculated weight of 2.588, accounting for 60.5% of the total, as shown in Figure 7 (a). In contrast, low-level visual cortex (LVC, such as V1, V2, V3) have a weight of 1.685, representing 39.5%. Although it is not immediately apparent from Figure 6 (b) which ROI contributes most to the decoding of structural feature, Figure 7 (b) reveals that V1 and V2 have the greatest weight, with HVC having a weight of 1.279 (36.03%), and LVC weighing 2.271 (63.97%). Considering the aforementioned findings, our results are plausible from the perspective of cognitive neuroscience. It is generally believed that LVC is predominantly responsible for processing low-level information of visual stimuli [4, 54, 55], such as orientation and contour. Meanwhile, V4 is involved in color processing [56, 57]. In contrast, HVC is responsible for processing high-level semantic information of objects[58], including category.

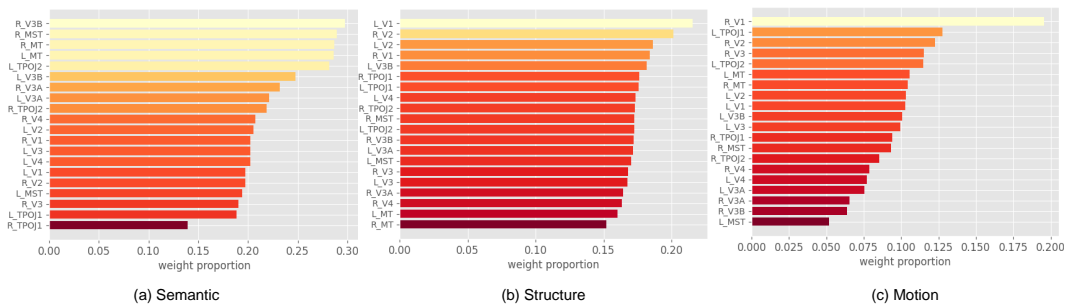


Figure 7: **ROI-wise** importance maps in the visual cortex of subject 1.

Figure 6 (c) indicates that both LVC and HVC contribute to the decoding of motion information, with significant weight attributed to V1 and MT. As derived from Figure 7 (c), the weight distribution between LVC and HVC is comparable, accounting for 42.4% and 57.6%, respectively. This observation is consistent with previous work[59], which validates the function of MT in visual motion processing. Furthermore, our findings affirm that the spatial and temporal modules designed in CMG effectively capture spatiotemporal information from across both LVC and HVC.

6 Conclusion

In this paper, we introduce a video reconstruction model (Mind-Animator) that decouples semantic, structural, and motion information from fMRI, achieving state-of-the-art performance across 3 public

datasets. We mitigate the interference of external video data on motion information decoding through a rational experimental design. The results of the permutation test demonstrate that the motion information we decoded indeed originates from fMRI, rather than being a "hallucination" from generative model. Additionally, the visualization of voxel-wise and ROI-wise importance maps substantiate the neurobiological interpretability of our model.

Acknowledgments and Disclosure of Funding

We would like to express our gratitude to Prof. Jack L. Gallant and Prof. Shinji Nishimoto for their pioneering exploration in the field of video reconstruction and for their high-quality code. We are grateful to Prof. Juan Helen Zhou and Dr. Zijiao Chen for their patient answers to our questions and for making all the results of the Mind-video test set public. We also extend our thanks to Prof. Michal Irani, Dr. Ganit Kupersmidt, and Dr. Roman Belyi for providing us with all the reconstruction results of their models on the test set.

We would like to express our appreciation to Prof. Zhongming Liu and Dr. Haiguang Wen for their open-sourced high-quality video-fMRI dataset and the preprocessing procedures. Our gratitude also goes to the Human Connectome Project (HCP) for providing a large-scale fMRI dataset and cortical visualization tools. We are thankful to the Algonauts2021 competition for providing a set of pre-processed video-fMRI data from multiple subjects.

We are thankful to the Stable Diffusion team for their high-performance text-to-image model, and we also appreciate the Tune-a-video team for their open-source video editing framework, which allows us to reconstruct videos without introducing additional motion information.

References

- [1] Simone Palazzo, Concetto Spampinato, Isaak Kavasidis, Daniela Giordano, Joseph Schmidt, and Mubarak Shah. Decoding brain representations by multimodal learning of neural activity and visual features. *IEEE Transactions on Pattern Analysis and Machine Intelligence*, 43(11):3833–3849, 2021.
- [2] Changde Du, Kaicheng Fu, Jinpeng Li, and Huiguang He. Decoding Visual Neural Representations by Multimodal Learning of Brain-Visual-Linguistic Features. *IEEE Transactions on Pattern Analysis and Machine Intelligence*, pages 1–17, 2023.
- [3] Elahe' Yargholi and Gholam-Ali Hossein-Zadeh. Brain decoding-classification of hand written digits from fMRI data employing Bayesian networks. *Frontiers in human neuroscience*, 10:351, 2016.
- [4] Kendrick N Kay, Thomas Naselaris, Ryan J Prenger, and Jack L Gallant. Identifying natural images from human brain activity. *Nature*, 452(7185):352–355, 2008.
- [5] Saudamini Roy Damarla and Marcel Adam Just. Decoding the representation of numerical values from brain activation patterns. *Human brain mapping*, 34(10):2624–2634, 2013.
- [6] Changde Du, Changying Du, Lijie Huang, Haibao Wang, and Huiguang He. Structured neural decoding with multitask transfer learning of deep neural network representations. *IEEE Transactions on Neural Networks and Learning Systems*, 33(2):600–614, 2020.
- [7] Tomoyasu Horikawa and Yukiyasu Kamitani. Generic decoding of seen and imagined objects using hierarchical visual features. *Nature communications*, 8(1):15037, 2017.
- [8] Yusuke Fujiwara, Yoichi Miyawaki, and Yukiyasu Kamitani. Modular encoding and decoding models derived from Bayesian canonical correlation analysis. *Neural computation*, 25(4):979–1005, 2013.
- [9] Dirk Wildgruber, Axel Riecker, Ingo Hertrich, Michael Erb, Wolfgang Grodd, Thomas Ethofer, and Hermann Ackermann. Identification of emotional intonation evaluated by fmri. *Neuroimage*, 24(4):1233–1241, 2005.

- [10] Pierre Bellec, Vincent Perlbarg, Saâd Jbabdi, Mélanie Pélégrini-Issac, Jean-Luc Anton, Julien Doyon, and Habib Benali. Identification of large-scale networks in the brain using fmri. *Neuroimage*, 29(4):1231–1243, 2006.
- [11] Alard Roebroeck, Elia Formisano, and Rainer Goebel. The identification of interacting networks in the brain using fmri: model selection, causality and deconvolution. *Neuroimage*, 58(2):296–302, 2011.
- [12] Thomas Naselaris, Ryan J Prenger, Kendrick N Kay, Michael Oliver, and Jack L Gallant. Bayesian reconstruction of natural images from human brain activity. *Neuron*, 63(6):902–915, 2009.
- [13] Marcel AJ Van Gerven, Botond Cseke, Floris P De Lange, and Tom Heskes. Efficient Bayesian multivariate fMRI analysis using a sparsifying spatio-temporal prior. *NeuroImage*, 50(1):150–161, 2010.
- [14] Guohua Shen, Tomoyasu Horikawa, Kei Majima, and Yukiyasu Kamitani. Deep image reconstruction from human brain activity. *PLoS computational biology*, 15(1):e1006633, 2019.
- [15] Yizhuo Lu, Changde Du, Qiongyi Zhou, Dianpeng Wang, and Huiguang He. Minddiffuser: Controlled image reconstruction from human brain activity with semantic and structural diffusion. In *Proceedings of the 31st ACM International Conference on Multimedia*, pages 5899–5908, 2023.
- [16] Sikun Lin, Thomas Sprague, and Ambuj K Singh. Mind Reader: Reconstructing complex images from brain activities. *arXiv preprint arXiv:2210.01769*, 2022.
- [17] Guohua Shen, Kshitij Dwivedi, Kei Majima, Tomoyasu Horikawa, and Yukiyasu Kamitani. End-to-end deep image reconstruction from human brain activity. *Frontiers in Computational Neuroscience*, 13, 2019.
- [18] Changde Du, Changying Du, Lijie Huang, and Huiguang He. Conditional generative neural decoding with structured CNN feature prediction. In *Proceedings of the AAAI Conference on Artificial Intelligence*, volume 34, pages 2629–2636, 2020.
- [19] Zijiao Chen, Jiabin Qing, Tiange Xiang, Wan Lin Yue, and Juan Helen Zhou. Seeing Beyond the Brain: Conditional Diffusion Model with Sparse Masked Modeling for Vision Decoding. *arXiv preprint arXiv:2211.06956*, 2022.
- [20] Yu Takagi and Shinji Nishimoto. High-resolution image reconstruction with latent diffusion models from human brain activity. *bioRxiv*, pages 2022–11, 2022.
- [21] Furkan Ozelik, Bhavin Choksi, Milad Mozafari, Leila Reddy, and Rufin VanRullen. Reconstruction of perceived images from fMRI patterns and semantic brain exploration using instance-conditioned GANs. In *2022 International Joint Conference on Neural Networks (IJCNN)*, pages 1–8. IEEE, 2022.
- [22] Roman Belyi, Guy Gaziv, Assaf Hoogi, Francesca Strappini, Tal Golan, and Michal Irani. From voxels to pixels and back: Self-supervision in natural-image reconstruction from fMRI. *Advances in Neural Information Processing Systems*, 32, 2019.
- [23] Leslie G Ungerleider and James V Haxby. ‘what’ and ‘where’ in the human brain. *Current opinion in neurobiology*, 4(2):157–165, 1994.
- [24] Alomit Ishai, Leslie G Ungerleider, Alex Martin, Jennifer L Schouten, and James V Haxby. Distributed representation of objects in the human ventral visual pathway. *Proceedings of the National Academy of Sciences*, 96(16):9379–9384, 1999.
- [25] Mortimer Mishkin, Leslie G Ungerleider, and Kathleen A Macko. Object vision and spatial vision: two cortical pathways. *Trends in neurosciences*, 6:414–417, 1983.
- [26] Nikos K Logothetis. The neural basis of the blood–oxygen–level–dependent functional magnetic resonance imaging signal. *Philosophical Transactions of the Royal Society of London. Series B: Biological Sciences*, 357(1424):1003–1037, 2002.

- [27] Seong-Gi Kim and Seiji Ogawa. Biophysical and physiological origins of blood oxygenation level-dependent fmri signals. *Journal of Cerebral Blood Flow & Metabolism*, 32(7):1188–1206, 2012.
- [28] Shinji Nishimoto, An T Vu, Thomas Naselaris, Yuval Benjamini, Bin Yu, and Jack L Gallant. Reconstructing visual experiences from brain activity evoked by natural movies. *Current biology*, 21(19):1641–1646, 2011.
- [29] Edward H Adelson and James R Bergen. Spatiotemporal energy models for the perception of motion. *Josa a*, 2(2):284–299, 1985.
- [30] Kuan Han, Haiguang Wen, Junxing Shi, Kun-Han Lu, Yizhen Zhang, Di Fu, and Zhongming Liu. Variational autoencoder: An unsupervised model for encoding and decoding fmri activity in visual cortex. *NeuroImage*, 198:125–136, 2019.
- [31] Haiguang Wen, Junxing Shi, Yizhen Zhang, Kun-Han Lu, Jiayue Cao, and Zhongming Liu. Neural encoding and decoding with deep learning for dynamic natural vision. *Cerebral cortex*, 28(12):4136–4160, 2018.
- [32] Chong Wang, Hongmei Yan, Wei Huang, Jiye Li, Yuting Wang, Yun-Shuang Fan, Wei Sheng, Tao Liu, Rong Li, and Huaifu Chen. Reconstructing rapid natural vision with fmri-conditional video generative adversarial network. *Cerebral Cortex*, 32(20):4502–4511, 2022.
- [33] Ian Goodfellow, Jean Pouget-Abadie, Mehdi Mirza, Bing Xu, David Warde-Farley, Sherjil Ozair, Aaron Courville, and Yoshua Bengio. Generative adversarial networks. *Communications of the ACM*, 63(11):139–144, 2020.
- [34] Ganit Kupershmidt, Roman Belyi, Guy Gaziv, and Michal Irani. A penny for your (visual) thoughts: Self-supervised reconstruction of natural movies from brain activity. *arXiv preprint arXiv:2206.03544*, 2022.
- [35] Milan Ilic. Auto-encoding variational bayes. 2019.
- [36] Zijiao Chen, Jiaxin Qing, and Juan Helen Zhou. Cinematic mindscapes: High-quality video reconstruction from brain activity. *Advances in Neural Information Processing Systems*, 36, 2024.
- [37] Alec Radford, Jong Wook Kim, Chris Hallacy, Aditya Ramesh, Gabriel Goh, Sandhini Agarwal, Girish Sastry, Amanda Askell, Pamela Mishkin, Jack Clark, et al. Learning transferable visual models from natural language supervision. In *International conference on machine learning*, pages 8748–8763. PMLR, 2021.
- [38] Robin Rombach, Andreas Blattmann, Dominik Lorenz, Patrick Esser, and Björn Ommer. High-resolution image synthesis with latent diffusion models. In *Proceedings of the IEEE/CVF Conference on Computer Vision and Pattern Recognition*, pages 10684–10695, 2022.
- [39] Jay Zhangjie Wu, Yixiao Ge, Xintao Wang, Stan Weixian Lei, Yuchao Gu, Yufei Shi, Wynne Hsu, Ying Shan, Xiaohu Qie, and Mike Zheng Shou. Tune-a-video: One-shot tuning of image diffusion models for text-to-video generation. In *Proceedings of the IEEE/CVF International Conference on Computer Vision*, pages 7623–7633, 2023.
- [40] Aaron Van Den Oord, Oriol Vinyals, et al. Neural discrete representation learning. *Advances in neural information processing systems*, 30, 2017.
- [41] Ashish Vaswani, Noam Shazeer, Niki Parmar, Jakob Uszkoreit, Llion Jones, Aidan N Gomez, Łukasz Kaiser, and Illia Polosukhin. Attention is all you need. *Advances in neural information processing systems*, 30, 2017.
- [42] Paul Scotti, Atmadeep Banerjee, Jimmie Goode, Stepan Shabalina, Alex Nguyen, Aidan Dempster, Nathalie Verlinde, Elad Yundler, David Weisberg, Kenneth Norman, et al. Reconstructing the mind’s eye: fmri-to-image with contrastive learning and diffusion priors. *Advances in Neural Information Processing Systems*, 36, 2024.

- [43] Chengying Gao, Qi Liu, Qi Xu, Limin Wang, Jianzhuang Liu, and Changqing Zou. Sketchycoco: Image generation from freehand scene sketches. In *Proceedings of the IEEE/CVF conference on computer vision and pattern recognition*, pages 5174–5183, 2020.
- [44] Aria Y. Wang, Kendrick Kay, Thomas Naselaris, Michael J. Tarr, and Leila Wehbe. Incorporating natural language into vision models improves prediction and understanding of higher visual cortex. *bioRxiv*, 2022.
- [45] Qiongyi Zhou, Changde Du, Shengpei Wang, and Huiguang He. Clip-mused: Clip-guided multi-subject visual neural information semantic decoding. *arXiv preprint arXiv:2402.08994*, 2024.
- [46] Joao Carreira and Andrew Zisserman. Quo vadis, action recognition? a new model and the kinetics dataset. In *proceedings of the IEEE Conference on Computer Vision and Pattern Recognition*, pages 6299–6308, 2017.
- [47] Levon Khachatryan, Andranik Movsisyan, Vahram Tadevosyan, Roberto Henschel, Zhangyang Wang, Shant Navasardyan, and Humphrey Shi. Text2video-zero: Text-to-image diffusion models are zero-shot video generators. In *Proceedings of the IEEE/CVF International Conference on Computer Vision*, pages 15954–15964, 2023.
- [48] Daniel S Marcus, John Harwell, Timothy Olsen, Michael Hodge, Matthew F Glasser, Fred Prior, Mark Jenkinson, Timothy Laumann, Sandra W Curtiss, and David C Van Essen. Informatics and data mining tools and strategies for the human connectome project. *Frontiers in neuroinformatics*, 5:4, 2011.
- [49] Radoslaw Martin Cichy, Kshitij Dwivedi, Benjamin Lahner, Alex Lascelles, Polina Iamshchikina, Monika Graumann, Alex Andonian, NAR Murty, K Kay, Gemma Roig, et al. The algonauts project 2021 challenge: How the human brain makes sense of a world in motion. *arXiv preprint arXiv:2104.13714*, 2021.
- [50] Alexey Dosovitskiy, Lucas Beyer, Alexander Kolesnikov, Dirk Weissenborn, Xiaohua Zhai, Thomas Unterthiner, Mostafa Dehghani, Matthias Minderer, Georg Heigold, Sylvain Gelly, et al. An image is worth 16x16 words: Transformers for image recognition at scale. *arXiv preprint arXiv:2010.11929*, 2020.
- [51] Jia Deng, Wei Dong, Richard Socher, Li-Jia Li, Kai Li, and Li Fei-Fei. Imagenet: A large-scale hierarchical image database. In *2009 IEEE Conference on Computer Vision and Pattern Recognition*, pages 248–255, 2009.
- [52] Zhan Tong, Yibing Song, Jue Wang, and Limin Wang. Videomae: Masked autoencoders are data-efficient learners for self-supervised video pre-training. *Advances in neural information processing systems*, 35:10078–10093, 2022.
- [53] Hanoona Rasheed, Muhammad Uzair Khattak, Muhammad Maaz, Salman Khan, and Fahad Shahbaz Khan. Fine-tuned clip models are efficient video learners. In *Proceedings of the IEEE/CVF Conference on Computer Vision and Pattern Recognition*, pages 6545–6554, 2023.
- [54] John-Dylan Haynes and Geraint Rees. Predicting the orientation of invisible stimuli from activity in human primary visual cortex. *Nature neuroscience*, 8(5):686–691, 2005.
- [55] Yukiyasu Kamitani and Frank Tong. Decoding the visual and subjective contents of the human brain. *Nature neuroscience*, 8(5):679–685, 2005.
- [56] Julia A Nunn, Lloyd J Gregory, Michael Brammer, Steven CR Williams, David M Parslow, Michael J Morgan, Robin G Morris, Edward T Bullmore, Simon Baron-Cohen, and Jeffrey Alan Gray. Functional magnetic resonance imaging of synesthesia: activation of v4/v8 by spoken words. *Nature neuroscience*, 5(4):371–375, 2002.
- [57] Hisashi Tanigawa, Haidong D Lu, and Anna W Roe. Functional organization for color and orientation in macaque v4. *Nature neuroscience*, 13(12):1542–1548, 2010.
- [58] James J DiCarlo, Davide Zoccolan, and Nicole C Rust. How does the brain solve visual object recognition? *Neuron*, 73(3):415–434, 2012.

- [59] Richard T Born and David C Bradley. Structure and function of visual area mt. *Annu. Rev. Neurosci.*, 28:157–189, 2005.
- [60] James V Haxby, M Ida Gobbini, Maura L Furey, Alomit Ishai, Jennifer L Schouten, and Pietro Pietrini. Distributed and overlapping representations of faces and objects in ventral temporal cortex. *Science*, 293(5539):2425–2430, 2001.
- [61] KN Kay, Naselaris T, Prenger RJ, Gallant JL. *Identifying natural images from human brain activity*. *nature*, 452:352–355, 2008.
- [62] Olivier Chapelle, Bernhard Scholkopf, and Alexander Zien. Semi-supervised learning (chappelle, o. et al., eds.; 2006)[book reviews]. *IEEE Transactions on Neural Networks*, 20(3):542–542, 2009.
- [63] Guy Gaziv, Roman Belyi, Niv Granot, Assaf Hoogi, Francesca Strappini, Tal Golan, and Michal Irani. Self-supervised natural image reconstruction and large-scale semantic classification from brain activity. *NeuroImage*, 254:119121, 2022.
- [64] Kaiming He, Xinlei Chen, Saining Xie, Yanghao Li, Piotr Dollár, and Ross Girshick. Masked autoencoders are scalable vision learners. In *Proceedings of the IEEE/CVF Conference on Computer Vision and Pattern Recognition*, pages 16000–16009, 2022.
- [65] Zijin Gu, Keith Jamison, Amy Kuceyeski, and Mert Sabuncu. Decoding natural image stimuli from fMRI data with a surface-based convolutional network. *arXiv preprint arXiv:2212.02409*, 2022.
- [66] Johannes G Wijmans and Richard W Baker. The solution-diffusion model: a review. *Journal of membrane science*, 107(1-2):1–21, 1995.
- [67] Jonathan Ho, Ajay Jain, and Pieter Abbeel. Denoising diffusion probabilistic models. *Advances in neural information processing systems*, 33:6840–6851, 2020.
- [68] Olaf Ronneberger, Philipp Fischer, and Thomas Brox. U-net: Convolutional networks for biomedical image segmentation. In *Medical Image Computing and Computer-Assisted Intervention–MICCAI 2015: 18th International Conference, Munich, Germany, October 5–9, 2015, Proceedings, Part III 18*, pages 234–241. Springer, 2015.
- [69] Jonathan Ho, Tim Salimans, Alexey Gritsenko, William Chan, Mohammad Norouzi, and David J Fleet. Video diffusion models. *Advances in Neural Information Processing Systems*, 35:8633–8646, 2022.
- [70] Jonathan Ho, William Chan, Chitwan Saharia, Jay Whang, Ruiqi Gao, Alexey Gritsenko, Diederik P Kingma, Ben Poole, Mohammad Norouzi, David J Fleet, et al. Imagen video: High definition video generation with diffusion models. *arXiv preprint arXiv:2210.02303*, 2022.
- [71] Uriel Singer, Adam Polyak, Thomas Hayes, Xi Yin, Jie An, Songyang Zhang, Qiyuan Hu, Harry Yang, Oron Ashual, Oran Gafni, et al. Make-a-video: Text-to-video generation without text-video data. *arXiv preprint arXiv:2209.14792*, 2022.
- [72] Daquan Zhou, Weimin Wang, Hanshu Yan, Weiwei Lv, Yizhe Zhu, and Jiashi Feng. Magicvideo: Efficient video generation with latent diffusion models. *arXiv preprint arXiv:2211.11018*, 2022.
- [73] Yingqing He, Tianyu Yang, Yong Zhang, Ying Shan, and Qifeng Chen. Latent video diffusion models for high-fidelity long video generation. *arXiv preprint arXiv:2211.13221*, 2022.
- [74] Junnan Li, Dongxu Li, Silvio Savarese, and Steven Hoi. Blip-2: Bootstrapping language-image pre-training with frozen image encoders and large language models. In *International conference on machine learning*, pages 19730–19742. PMLR, 2023.
- [75] Matthew F Glasser, Timothy S Coalson, Emma C Robinson, Carl D Hacker, John Harwell, Essa Yacoub, Kamil Ugurbil, Jesper Andersson, Christian F Beckmann, Mark Jenkinson, et al. A multi-modal parcellation of human cerebral cortex. *Nature*, 536(7615):171–178, 2016.
- [76] Beichen Zhang, Pan Zhang, Xiaoyi Dong, Yuhang Zang, and Jiaqi Wang. Long-clip: Unlocking the long-text capability of clip. *arXiv preprint arXiv:2403.15378*, 2024.

Animate Your Thoughts: Decoupled Reconstruction of Dynamic Natural Vision from Slow Brain Activity

Appendix

Contents

1	Introduction	1
2	Methodology	3
2.1	Overview	3
2.2	Problem Statement	3
2.3	fMRI-to-feature Stage	4
2.4	Feature-to-video Stage	5
3	Experiment	6
3.1	Datasets	6
3.2	Evaluation Metrics	6
4	Results	6
4.1	Comparative Experimental Results	6
4.2	Ablation Study	7
5	Interpretability Analysis	8
5.1	Have we truly decoded motion information from fMRI?	8
5.2	Which brain regions are responsible for decoding different features, respectively?	8
6	Conclusion	9
A	Related Work	17
A.1	Reconstructing Human Vision from Brain Activities	17
A.2	Diffusion Models	17
A.3	Diffusion Models for Video Generation	18
B	Model Architecture	18
B.1	Consistency Motion Generator	18
B.2	Text-to-Image Network Inflation	19
C	Data Preprocessing	19
C.1	Video Captioning with BLIP2	19
C.2	CC2017	19
C.3	HCP	19
C.4	Algonauts2021	20

C.5	Data Acquisition	21
D	Implementation Details	21
D.1	Hyperparameter Settings	21
D.2	Evaluation Metric Implementation	22
E	Additional Experimental Results	22
E.1	Further Results on the CC2017 Dataset	22
E.1.1	CC2017 sub2	23
E.1.2	CC2017 sub3	23
E.1.3	More Reconstruction Results on Multiple Subjects	23
E.2	Further Results on the HCP Dataset	25
E.3	Further Results on the Algonauts2021 Dataset	25
E.4	A Detailed Ablation Study on Various Hyperparameters	27
E.5	Further Results on Interpretability Analysis	28
F	Limitations and Future Work	28
G	Broader Impacts	29

A Related Work

A.1 Reconstructing Human Vision from Brain Activities

Reconstructing Images from Brain Activities

Building on Haxby’s[60] seminal work, the field of neural decoding has seen a proliferation of tasks with significant implications for guiding research. These tasks can be broadly classified into three categories: stimulus classification, identification, and reconstruction, with the latter being the most challenging and the focus of our study.

Traditional image reconstruction techniques rely on linear regression models to correlate fMRI with manually defined image features[8, 12, 61], yielding blurry results and a heavy reliance on manual feature selection. However, the advent of deep learning has revolutionized this domain. Deep neural networks (DNNs) have become increasingly prevalent for their ability to address the scarcity of stimulus-fMRI pairs through semi-supervised learning[62], as demonstrated by Beliy et al.[22] and Gaziv et al.[63]. Yet, these models often fail to capture discernible semantic information. Chen et al.[19] employed a pre-training and fine-tuning approach on fMRI data, leveraging methods akin to Masked Autoencoder(MAE)[64] and Latent Diffusion Models(LDM)[38] to improve reconstruction quality. Ozcelik et al.[21] and Gu et al.[65] utilized self-supervised models for feature extraction, followed by iterative optimization to refine the reconstruction process. The integration of semantic information from text, facilitated by Contrastive Language-Image Pre-Training (CLIP)[37], has been instrumental in reconstructing complex natural images. Lin et al.[16] and Takagi et al.[20] demonstrated the potential of aligning fMRI with CLIP representations and mapping fMRI to text and image features for high-fidelity reconstruction.

While rapid advancements have been made in stimulus reconstruction, with some researchers achieving reconstructions from brain signals that closely approximate the original stimuli, the majority of prior work has focused on static image reconstruction. This study, however, shifts the focus to the more challenging task of video reconstruction.

Reconstructing Videos from Brain Activities

Compared to image reconstruction, the challenge in video reconstruction lies in the significant discrepancy between the temporal resolution of fMRI (0.5Hz) and the frame rate of the stimulus video (30Hz), which presents a substantial challenge in modeling the mapping between fMRI signals and video content. To overcome the challenge, Nishimoto [28] transformed the video reconstruction task into an identification problem, employing the Motion-Energy model [29] and Bayesian inference to reconstruct videos from a predefined video library. Subsequently, Han [30] and Wen et al.[31] mapped brain responses to the feature spaces of DNN to reconstruct down-sampled (with the frame rate reduced to 1Hz) video stimuli. The aforementioned studies have preliminarily validated the feasibility of reconstructing video frames from fMRI. Wang et al.[32] developed an f-CVGAN that learns temporal and spatial information in fMRI through separate discriminators [33]. To mitigate the scarcity of fMRI-video data, Kupersmidt et al.[34] utilized self-supervised learning [35] to incorporate a large amount of unpaired video data. These efforts have validated the feasibility of video reconstruction from fMRI, albeit with a lack of explicit semantic information in the results. Chen et al.[36] utilized contrastive learning to map fMRI to the CLIP representation space and fine-tuned inflated Stable Diffusion [38, 39] on a video-text dataset as a video generation model, successfully reconstructing coherent videos with clear semantic information for the first time. However, Chen did not consider structure information such as color and position, and it was uncertain whether the motion information in the reconstructed videos originated from the fMRI or the video generation model.

A.2 Diffusion Models

Diffusion models[66, 67], a class of probabilistic generative models, have increasingly rivaled or surpassed the performance of Generative Adversarial Networks (GAN)[33] in specific tasks within the field of computer vision. Diffusion models encompass a forward diffusion process and a reverse denoising process, each exhibiting Markovian behavior. The forward process incrementally introduces Gaussian noise into the original image, culminating in a transition to standard Gaussian noise. The

forward diffusion process can be represented as $q(x_t|x_{t-1}) = N(x_t; \sqrt{\alpha_t}x_{t-1}, (1 - \alpha_t)I)$, where t denotes the time step of each noise addition. The reverse denoising process employs the U-Net[68] architecture to accurately model the noise distribution at each timestep t . The image synthesis is achieved through a sequential denoising and sampling procedure, initiated from standard Gaussian noise.

In the context of image generation tasks, the conventional diffusion model executes two Markov processes in a large pixel space, resulting in substantial computational resource utilization. To address this issue, Latent Diffusion Models (LDM)[38] employs a VQ-VAE[40] encoder to transform the pixel space into a low-dimensional latent space. Subsequently, the diffusion model’s training and generation are performed in the latent space, with the final generated image obtained by utilizing the VQ-VAE decoder. This approach significantly reduces computational resource requirements and inference time while preserving the quality of generated images.

A.3 Diffusion Models for Video Generation

After achieving significant progress in text-to-image (T2I) generation tasks, diffusion models have piqued the interest of researchers in exploring their potential for text-to-video (T2V) generation. The pioneering work by Ho et al.[69], introducing the 3D diffusion U-Net, marked significant progress in applying Diffusion Models to video generation. This was followed by further advancements by Ho et al.[70], who utilized a cascaded sampling framework and super-resolution method to generate high-resolution videos. Subsequent contributions have expanded upon this work, notably with the incorporation of a temporal attention mechanism over frames by Singer et al.[71] in Make-A-Video. Zhou et al.[72] with MagicVideo, and He et al.[73] with LVDM, have integrated this mechanism into latent Diffusion Models, significantly enhancing video generation capabilities. However, due to the scarcity of paired text-video datasets and the high memory requirements for training 3D U-Nets, alternative approaches are being explored. These involve refining pre-trained T2I models to directly undertake T2V tasks. Khachatryan et al.[47] introduced two enhancements to enable zero-shot adaptation of T2I models to T2V tasks: (1) the implementation of cross-frame attention, ensuring that the generation of each current frame in a video considers information from preceding frames; and (2) the consideration of inter-frame correlations during noise sampling, rather than random sampling for each frame independently. Wu et al.[39] also employed cross-frame attention and achieved one-shot video editing by fine-tuning partial model parameters on individual videos.

In this work, tasked with video reconstruction from fMRI, we eschewed the use of pre-trained T2V models to mitigate the interference of external video data with the decoding of motion information from fMRI. Inspired by the cross-frame attention mechanism, we adapted a T2I model through network inflation techniques, enabling it to generate multi-frame videos. Consequently, the generative model employed in our study has never been exposed to video data, ensuring that the motion information in the reconstructed videos is solely derived from the fMRI decoding process.

B Model Architecture

B.1 Consistency Motion Generator

Figure 3 illustrates the Consistency Motion Generator, which is primarily composed of two modules: the Temporal Module and the Spatial Module.

The Temporal Module is tasked with learning the temporal dynamics from the visible frames. Given the severe information redundancy between video frame tokens, we specifically design a Sparse Causal mask. As shown in Figure 3 on the right, during training, the mask is divided into **fixed** and **random** components. The fixed mask ensures that each frame cannot access information from subsequent frames, while the random mask maintains sparsity among visible frames, preventing the model from taking shortcuts[52] and accelerating training. During inference, we eliminate the random mask to allow full utilization of information from all preceding frames for predicting future frames.

Since a single fMRI frame captures information from several video frames, we design a cross attention mechanism within the Spatial Module to extract the necessary temporal and spatial information for predicting the next frame token from the fMRI data.

B.2 Text-to-Image Network Inflation

To leverage pre-trained weights from large-scale image datasets, such as ImageNet, for the pre-training of massive video understanding models, Carreira et al.[46] pioneered the expansion of filters and pooling kernels in 2D ConvNets into the third dimension to create 3D filters and pooling kernels. This process transforms $N \times N$ filters used for images into $N \times N \times N$ 3D filters, providing a beneficial starting point for 3D video understanding models by utilizing spatial features learned from large-scale image datasets.

In the field of generative model, several attempts have been made to extend generative image models to video models. A key technique employed in this work involves augmenting the Query, Key, and Value of the attention module, as illustrated below:

$$Q = W^Q \cdot z_{v_i}, \quad K = W^K \cdot [z_{v_0}, z_{v_{i-1}}], \quad V = W^V \cdot [z_{v_0}, z_{v_{i-1}}], \quad (10)$$

where z_{v_i} denotes the latent of the i -th frame during the generation process.

C Data Preprocessing

For the stimulus videos of the three datasets described below, we segmented them into 2-second clips, down-sampled the frame rate to 4Hz (i.e., evenly extracting 8 frames), then centrally cropped each frame, and resized each to a shape of 512x512. Following the approach of Chen et al.[36], we employed BLIP2[74] to obtain textual descriptions for each video clip, with lengths not exceeding 20 words.

C.1 Video Captioning with BLIP2

PyTorch code for the video captioning process is depicted in Algorithm 1.

C.2 CC2017

CC2017[31] dataset was first used in the work of Wen et al.[31] This dataset include fMRI data from 3 subjects who view a variety of movie clips ($23^\circ \times 23^\circ$) with a central fixation cross ($0.8^\circ \times 0.8^\circ$). Clips are divided into 18 training movies and 5 testing movies, each eight minutes long, presented 2 and 10 times to each subject, respectively. MRI (T1 and T2-weighted) and fMRI data (2-second temporal resolution) are acquired using a 3-T system. The fMRI volumes are processed for artifact removal, motion correction (6 DOF), registered to MNI space, and projected onto cortical surfaces coregistered to a template.

To extract voxels in the activated visual areas, we calculate the correlation of the time series for each voxel’s activation across 2 trials within the training set. Subsequently, we apply Fisher’s z-transform to the computed correlations, average the results across 18 sessions, and identify the most significant 4500 voxels using a paired t-test to form a mask. This mask is computed separately for each of the 3 subjects on their respective training sets and then applied to both training and test set data, with the selected voxels averaged across trials. Following the work of Nishimoto et al.[28] and Han et al. [30], we utilize BOLD signals with a 4-second lag to represent the movie stimulus responses, thereby accounting for the hemodynamic response delay.

C.3 HCP

This dataset is part of the Human Connectome Project (HCP)[48], encompassing BOLD (blood-oxygen-level dependent) responses from 158 subjects. For the subsequent experiments, three subjects (100610, 102816, and 104416) are randomly selected from this dataset. Data acquisition is performed using a 7T MRI scanner with a spatial resolution of 1.6 millimeters and a repetition time (TR) of 1 second. The utilized BOLD signals undergo standard HCP preprocessing procedures, which include correction for head motion and distortion, high-pass filtering, and removal of temporal artifacts via independent component analysis (ICA). The preprocessed BOLD responses are then registered to the MNI standard space.

Due to the difficulty in directly acquiring fMRI data from multiple trials, we directly utilize the parcellation of the human cerebral cortex proposed by Glasser et al.[75] to extract voxels within

Algorithm 1: PyTorch code for the video captioning process

```
import torch
import clip
import random
import numpy as np
from PIL import Image
from lavis.models import load_model_and_preprocess

device = torch.device('cuda:5')
clip_model, clip_preprocess = clip.load("ViT-B/32", device=device)
model, vis_processors, _ = load_model_and_preprocess(name="blip2_t5",
model_type="pretrain_flant5xxl", is_eval=True, device=device)
prompt = "Question: What does this image describe? Answer:"

def Video_Captioning(Train_video_path_root):
    Train_Captions = []
    for i in tqdm(range(18)):
        for j in tqdm(range(240)):
            frames_root = Train_video_path_root + 'seg{}__{}/'.format(i+1, j+1)
            frame1 = Image.open(frames_root + '0000000.jpg').convert("RGB")
            frame1 = vis_processors["eval"](frame1).unsqueeze(0).to(device)
            frame2 = Image.open(frames_root + '0000056.jpg').convert("RGB")
            frame2 = vis_processors["eval"](frame2).unsqueeze(0).to(device)
            frame_mid = Image.open(frames_root + '0000024.jpg').convert("RGB")
            clip_image = clip_preprocess(frame_mid).unsqueeze(0).to(device)

            caption1 = model.generate({"image": frame1, "prompt": prompt})
            caption2 = model.generate({"image": frame2, "prompt": prompt})

            text1 = clip.tokenize(caption1).to(device)
            text2 = clip.tokenize(caption2).to(device)

            with torch.no_grad():
                image_features3 = clip_model.encode_image(clip_image)
                text_features1 = clip_model.encode_text(text1)
                text_features2 = clip_model.encode_text(text2)
                cos_sim1 = torch.cosine_similarity(image_features3, text_features1)
                cos_sim2 = torch.cosine_similarity(image_features3, text_features2)

            if abs(cos_sim1 - cos_sim2) <= 0.05:
                number = random.random()
                if number >= 0.5:
                    caption = caption1[0]
                else:
                    caption = caption2[0]
            else:
                caption = caption1[0] + ', and then ' + caption2[0]
            Train_Captions.append(caption)
    Train_Captions = np.array(Train_Captions)
    return Train_Captions
```

the activated visual cortex. The resulting ROIs we extract include: V1, V2, V3, hV4, PPA, FFA, LO, PHC, MT, MST, and TPOJ, totaling 5820 voxels. Following the work of Nishimoto et al.[28] and Han et al.[30], we utilize BOLD signals with a 4-second lag to represent the movie stimulus responses, thereby accounting for the hemodynamic response delay. Given that no prior work has conducted video reconstruction experiments on these three subjects from the HCP dataset, except for Wang et al.[32], we randomly shuffle all video segments and allocate 90% for the training set, with the remaining 10% reserved for the test set.

C.4 Algonauts2021

This dataset is publicly released for the 2021 Algonauts Challenge[49]. During data acquisition, 10 participants passively view 1100 silent videos of everyday events, each approximately 3 seconds in duration, presented three times. The participants' fMRI is recorded using a 3T Trio Siemens scanner with a spatial resolution of 2.5 millimeters and a repetition time (TR) of 1.75 seconds. The fMRI preprocessing involves steps such as slice-timing correction, realignment, coregistration, and normalization to the MNI space. Additionally, the fMRI data are interpolated to a TR of 2 seconds.

The dataset has been officially preprocessed, allowing us to extract brain responses from nine regions of interest (ROIs) within the visual cortex, including four primary and intermediate visual cortical areas V1, V2, V3, and V4, as well as five higher visual cortical areas: the Extrastriate Body Area (EBA), Fusiform Face Area (FFA), Superior Temporal Sulcus (STS), Lateral Occipital Cortex (LOC), and Parahippocampal Place Area (PPA). These areas selectively respond to body, face, biological

motion and facial information, objects, and scene information, respectively. In the experiment, the average neural response across three stimulus repetitions is taken for brain activity. As the test set data are not yet public, we utilize the first 900 sets of data for training and the 900-1000 sets for testing.

C.5 Data Acquisition

The open-source datasets used in this paper can be accessed via the following links:

- (1) CC2017: <https://purr.purdue.edu/publications/2809/1>
- (2) HCP: <https://www.humanconnectome.org/>
- (3) Algonauts2021: <http://algonauts.csail.mit.edu/2021/index.html>

D Implementation Details

D.1 Hyperparameter Settings

For all three datasets employed in the experiments, during the training of the Semantic Decoder, we set α to 0.5, λ_1 to 0.01, and λ_2 to 0.5. The batch size is set to 64, and the learning rate is set to $2e-4$, with training conducted 100 epochs. Given the critical role of data volume and augmentation methods in the training of contrastive learning models, and the scarcity of video-fMRI paired data, we implement specific data augmentation techniques to prevent overfitting. For fMRI data, we randomly select 20% of the voxels during each iteration, zero out 50% of their values. For image data, we randomly crop one frame from eight video frames to a size of 400×400 pixels, and then resize it to 224×224 . For text data, due to the presence of similar video clips in the training set (derived from a complete video segment), BLIP2 often provide identical textual descriptions, which leads to overfitting. To mitigate this, we apply more aggressive augmentation techniques. For an input sentence, we perform Synonym Replacement with a 50% probability and Random Insertion, Random Swap, and Random Deletion with a 20% probability each.

During the training of the Structural Decoder, we set the batch size to 64 and the learning rate to $1e-6$. To stabilize the learning process, we conduct the training process for 100 epochs with a 50-step warmup.

When training the Consistency Motion Generator, we set the mask ratio of the Sparse Causal mask to 0.6 during the training phase, with a batch size of 64 and a learning rate of $4e-5$. Similarly, for stability, we implement a 50-step warmup followed by 300 epochs of training.

Taking three subjects from the CC2017 dataset as an example, we utilize the first 4000 data points as the training set and the subsequent 320 data points as the validation set. Following this, we retrain the model on the entire training set, which comprises 4320 data points. The loss curve is depicted in Figure 8.

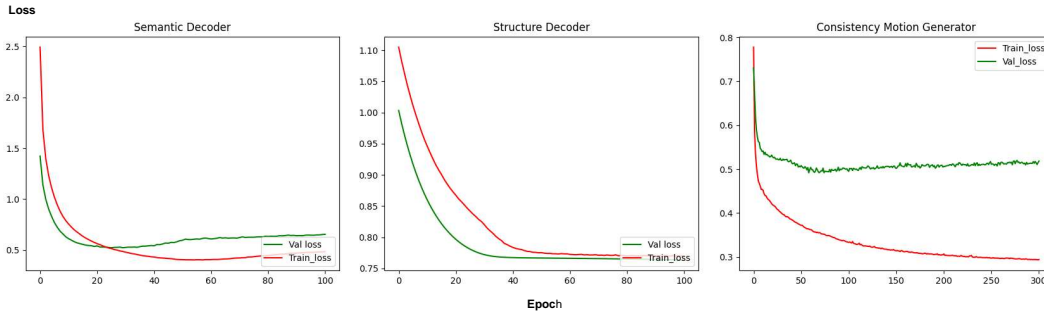


Figure 8: The training and validation loss curves for subject 1 in the CC2017 dataset.

According to Figure 8, in the inference phase, we utilize model parameters saved at the 30th, 75th, and 70th epochs for the Semantic Decoder, Structural Decoder, and Consistency Motion Generator,

respectively. For the generative model, we employ inflated Stable Diffusion V1-5. Given that Stable Diffusion operates on Gaussian-distributed latent space inputs (i.e., Z_T) for Text-to-Image task, and the distribution of decoded structural information does not align with this, we apply 250 steps of Gaussian smoothing to it, which includes 50 steps of ddim inversion. All experiments are conducted on a single A100 80G GPU, with the training phase taking 8 hours and the inference phase taking 12 hours for each dataset.

D.2 Evaluation Metric Implementation

Semantic-level

This algorithm performs the N-trial n-way top-1 classification test. We describe our evaluation method in Algorithm 2. For the image-based scenario, we utilize a Vision Transformer (ViT)[50] pre-trained on ImageNet as the classifier. For video-based scenario, a pre-trained VideoMAE[52] is employed as the classifier.

Algorithm 2: N-trial n-way top-1 classification test

```

1: Input pre-trained classifiers  $\mathcal{C}_{image}(\cdot)$ ,  $\mathcal{C}_{video}(\cdot)$ , video pair (Generated Video  $x$ , Corresponding
   GT Video  $\hat{x}$ ), mode(video-based or image-based)
2: Output success rate  $r \in [0, 1]$ 
3: if mode='video-based' then
4:   for  $N$  trials do
5:      $\hat{y} \leftarrow \mathcal{C}_{video}(\hat{x})$  get the ground-truth class
6:      $\{p_0, \dots, p_{399}\} \leftarrow \mathcal{C}_{video}(x)$  get the output probabilities
7:      $\{p_{\hat{y}}, p_{y_1}, \dots, p_{y_{n-1}}\} \leftarrow$  pick  $n-1$  random classes
8:     success if  $\arg \max_y \{p_{\hat{y}}, p_{y_1}, \dots, p_{y_{n-1}}\} = \hat{y}$ 
9:   end for
10:   $r =$  number of success /  $N$ 
11: else
12:  for 8 frames do
13:    for  $N$  trials do
14:       $\hat{y}_i \leftarrow \mathcal{C}_{image}(\hat{x}_i)$  get the ground-truth class
15:       $\{p_0, \dots, p_{999}\} \leftarrow \mathcal{C}_{image}(x_i)$  get the output probabilities
16:       $\{p_{\hat{y}_i}, p_{y_{i,1}}, \dots, p_{y_{i,n-1}}\} \leftarrow$  pick  $n-1$  random classes
17:      success if  $\arg \max_{y_i} \{p_{\hat{y}_i}, p_{y_{i,1}}, \dots, p_{y_{i,n-1}}\} = \hat{y}_i$ 
18:    end for
19:     $r_i =$  number of success /  $N$ 
20:  end for
21:   $r = \sum_{i=1}^8 r_i / 8$ 
22: end if

```

Spaciotemporal-level

Considering the input to the video reconstruction task contains substantial noise, there are instances where every pixel of each reconstructed video frame is either zero or noise, which would artificially inflate the CLIP score if used directly. Therefore, we calculate the CLIP score only when the VIFI-CLIP value exceeds 0.6; otherwise, we assign a score of 0.

E Additional Experimental Results

E.1 Further Results on the CC2017 Dataset

As depicted in Table 5 and 6, we further demonstrate the experimental results on subjects 2 and 3 from the CC2017 dataset. Specifically, for the metrics 2-way-I and 2-way-V, we present the mean and standard deviation across all samples over 100 trials, for the remaining metrics, we offer the

mean and standard deviation of all results within the test set to reflect the overall performance in reconstruction.

E.1.1 CC2017 sub2

As shown in Table 5, our model on subject 2 achieves SOTA performance in five out of seven metrics and secured second place in one.

	Semantic-level \uparrow			Pixel-level \uparrow			ST-level \uparrow
	2-way-I	2-way-V	VIFI-score	SSIM	PSNR	Hue-pcc	CLIP-pcc
Nishimoto[28]	0.787 \pm 0.04	—	—	0.112 \pm 0.07	8.592 \pm 2.11	0.713 \pm 0.11	—
Wen[31]	0.783 \pm 0.03	—	—	0.145 \pm 0.14	8.415 \pm 3.46	0.626 \pm 0.12	—
Wang[32]	0.727 \pm 0.04	0.779 \pm 0.03	<u>0.596\pm0.07</u>	0.107 \pm 0.06	<u>10.940\pm1.83</u>	0.589 \pm 0.19	0.404 \pm 0.38
Kupersmidt[34]	0.776 \pm 0.03	0.766 \pm 0.03	0.591 \pm 0.08	0.157 \pm 0.09	11.914\pm1.89	0.601 \pm 0.18	0.382 \pm 0.41
Chen[36]	<u>0.789\pm0.03</u>	0.842\pm0.03	0.595 \pm 0.08	<u>0.172\pm0.09</u>	8.929 \pm 1.62	<u>0.773\pm1.13</u>	<u>0.409\pm0.46</u>
Ours(sub2)	0.804\pm0.03	<u>0.832\pm0.03</u>	0.604\pm0.08	0.287\pm0.11	9.049 \pm 1.45	0.795\pm0.12	0.426\pm0.42

Table 5: Quantitative comparison of reconstruction results on subjects 2.

E.1.2 CC2017 sub3

As shown in Table 6, our model on subject 3 achieves SOTA performance in four out of seven metrics and secured second place in two. It should be noted that the primary objective of this work is to attempt the disentanglement of semantic, structural, and motion information from fMRI data, rather than achieving SOTA performance. The superior results obtained in the aforementioned metrics can more compellingly demonstrate the effectiveness of our proposed model.

	Semantic-level \uparrow			Pixel-level \uparrow			ST-level \uparrow
	2-way-I	2-way-V	VIFI-score	SSIM	PSNR	Hue-pcc	CLIP-pcc
Nishimoto[28]	0.712 \pm 0.04	—	—	0.128 \pm 0.07	8.546 \pm 1.91	0.746 \pm 0.12	—
Wen[31]	—	—	—	—	—	—	—
Wang[32]	0.722 \pm 0.04	0.778 \pm 0.03	0.584 \pm 0.07	0.098 \pm 0.06	<u>10.758\pm2.00</u>	0.572 \pm 0.49	0.392 \pm 0.41
Kupersmidt[34]	0.767 \pm 0.03	0.766 \pm 0.03	<u>0.597\pm0.08</u>	0.128 \pm 0.08	11.237\pm1.86	0.641 \pm 0.14	0.377 \pm 0.37
Chen[36]	0.811\pm0.03	0.848\pm0.03	0.597 \pm 0.08	<u>0.187\pm0.10</u>	9.013 \pm 1.66	<u>0.771\pm0.13</u>	<u>0.410\pm0.46</u>
Ours(sub3)	<u>0.792\pm0.03</u>	<u>0.833\pm0.02</u>	0.600\pm0.07	0.349\pm0.11	9.306 \pm 1.54	0.791\pm0.12	0.415\pm0.39

Table 6: Quantitative comparison of reconstruction results on subjects 3.

E.1.3 More Reconstruction Results on Multiple Subjects

Due to the anatomical and functional connectivity differences among subjects, even when presented with the same stimulus video, different brain signals are elicited. Consequently, we train the Mind-Animator on three subjects from the CC2017 dataset separately, with the reconstruction results shown in Figure 9. It can be observed that, despite training and applying the model directly to the three subjects without additional modifications, the reconstruction outcomes are largely consistent, which substantiates the effectiveness of our model.

However, as it is challenging to obtain a large volume of brain signals from the same subject, the direct extension of a model trained on one subject to others, or the direct training using data from multiple subjects, represents a future research direction that requires further investigation.

In Figure 10, we present additional reconstruction results from the CC2017 dataset, demonstrating that our model does not overfit despite the limited data volume. It is capable of decoding a rich array of video clips, such as two people conversing, an airplane in flight, and a dog turning its head, among others. These video clips encompass a wide range of natural scenarios found in everyday life, including human activities, animal behaviors, and natural landscapes.

Additionally, to provide a comprehensive and objective assessment of our model, we also include some reconstruction failure cases in Figure 11. The primary reasons for these failures are twofold.

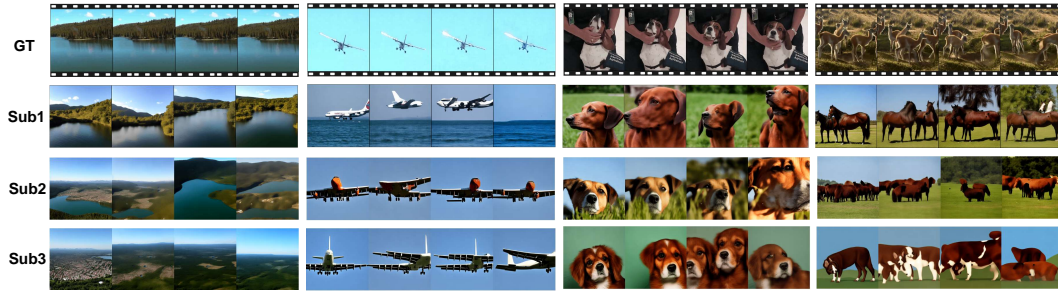


Figure 9: The reconstruction results on three subjects from the CC2017 dataset.

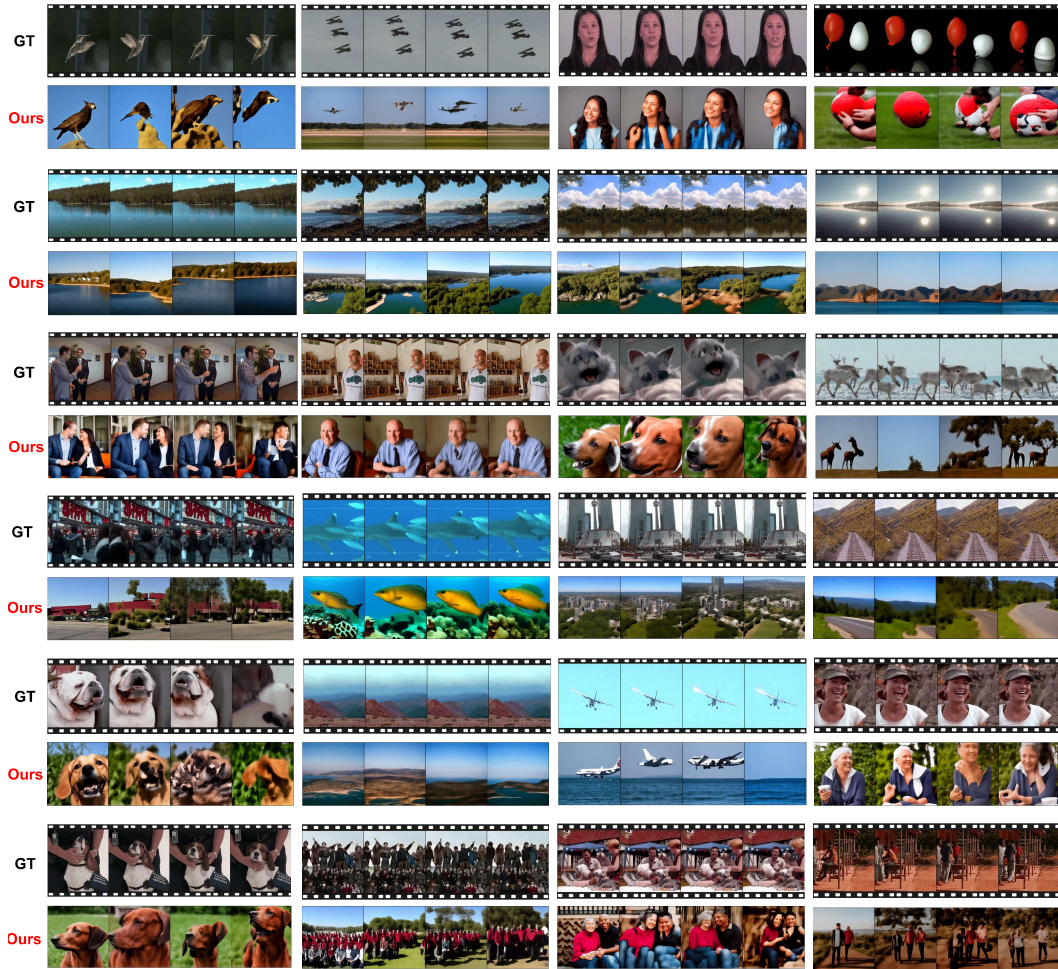


Figure 10: More reconstruction results on the CC2017 dataset.

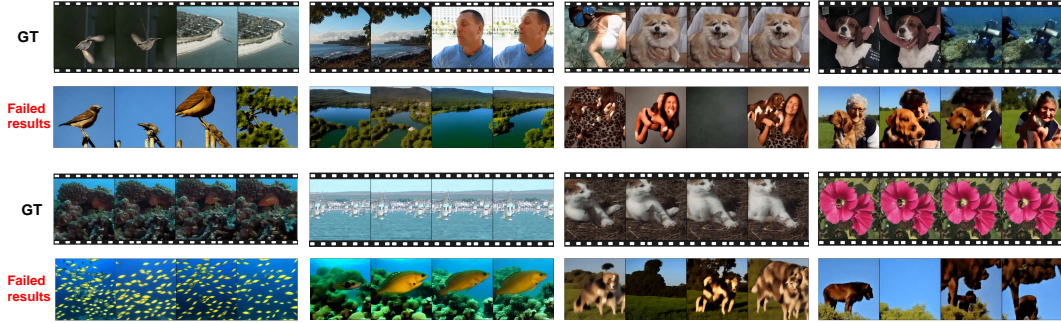


Figure 11: Reconstruction failure cases.

Firstly, the inherent data acquisition paradigm leads to abrupt transitions in content at the junction of video clips, which are evenly segmented from complete videos watched by the subjects during data collection. As illustrated in the first row of Figure 11, the model often struggles to recognize such abrupt changes, resulting in the reconstruction of only the scene prior to the transition. Secondly, errors in feature decoding occur, as shown in the second row of Figure 11. Although the model successfully decodes an ocean scene, structural decoding errors led to the appearance of numerous fish in the reconstructed frames.

E.2 Further Results on the HCP Dataset

To validate the broad effectiveness of our proposed model across different datasets, we also conduct experiments on the HCP dataset. The selection of three subjects (100610, 102816, and 104416) aligns with that of Wang et al.[32], and the parameter settings for Mind-Animator during both training and testing are identical to those used on the CC2017 dataset. We replicate Nishimoto et al.[28]’s model on HCP, utilizing video clips from the training sets of both CC2017 and HCP as video priors. Wang only reports SSIM and PSNR metrics on the HCP dataset. Visual comparisons are presented in Figure 12, while quantitative comparisons are detailed in Table 7. The results indicate that our model still performs well across multiple subjects in the HCP dataset.



Figure 12: The reconstruction results on three subjects from the HCP dataset.

E.3 Further Results on the Algonauts2021 Dataset

We conduct experiments on the Algonauts2021 competition dataset with 10 subjects, employing the same parameter settings for Mind-Animator during both training and testing as those used on the CC2017 dataset. Since no video reconstruction results has previously been published on this dataset, we replicate Nishimoto et al.’s model as a baseline and utilize video clips from the training sets of

Sub ID	Semantic-level \uparrow			Pixel-level \uparrow			ST-level \uparrow	
	2-way-I	2-way-V	VIFI-score	SSIM	PSNR	Hue-pcc	CLIP-pcc	
Sub01	Nishimoto[28]	0.658 \pm 0.04	—	—	0.307 \pm 0.14	11.711 \pm 2.12	0.649 \pm 0.12	—
	Wang[32]	—	—	—	0.154 \pm 0.11	13.200 \pm 4.01	—	—
	Ours	0.819 \pm 0.03	0.783 \pm 0.03	0.613 \pm 0.07	0.325 \pm 0.10	10.757 \pm 2.40	0.820 \pm 0.13	0.476 \pm 0.41
Sub02	Nishimoto[28]	0.661 \pm 0.04	—	—	0.338 \pm 0.14	11.249 \pm 2.17	0.643 \pm 0.12	—
	Wang[32]	—	—	—	0.178 \pm 0.11	13.700 \pm 5.00	—	—
	Ours	0.756 \pm 0.03	0.759 \pm 0.04	0.609 \pm 0.07	0.371 \pm 0.12	11.894 \pm 2.66	0.834 \pm 0.14	0.485 \pm 0.44
Sub03	Nishimoto[28]	0.657 \pm 0.04	—	—	0.319 \pm 0.14	10.988 \pm 2.14	0.645 \pm 0.13	—
	Wang[32]	—	—	—	0.147 \pm 0.11	12.200 \pm 4.00	—	—
	Ours	0.781 \pm 0.03	0.793 \pm 0.03	0.634 \pm 0.07	0.336 \pm 0.12	11.018 \pm 2.62	0.834 \pm 0.14	0.573 \pm 0.39

Table 7: Quantitative comparison of reconstruction results on HCP dataset.



Figure 13: The reconstruction results on four subjects from the Algonauts2021 dataset.

both CC2017 and HCP as video priors. Visual comparisons and quantitative assessments across various metrics are depicted in Figure 13 and detailed in Table 8, respectively. Although Table 8 indicates that our model outperforms the earlier baseline in nearly all metrics across the 10 subjects, the reconstructed results presented in Figure 13 are not entirely satisfactory, with some video frames semantically misaligned with the stimulus video. We attribute this to the scarcity of training data, which renders the video reconstruction task on this dataset challenging, given that the data volume per subject is approximately one-fifth of that in the CC2017 dataset.

Based on the experimental results across multiple datasets, we can draw the following conclusions: (1) The volume of training data from a single subject significantly influences the performance of current video reconstruction models, with greater sample size and data diversity leading to better reconstruction performance. (2) There is an urgent need to develop a new model using incremental learning or cross-subject learning methods that can be trained using data collected from different subjects, which we consider as a direction for future research.

Sub ID		Semantic-level \uparrow			Pixel-level \uparrow			ST-level \uparrow
		2-way-I	2-way-V	VIFI-score	SSIM	PSNR	Hue-pcc	CLIP-pcc
Sub01	Nishimoto[28]	0.688 \pm 0.04	—	—	0.446 \pm 0.08	9.626 \pm 1.61	0.672 \pm 0.15	—
	Ours	0.722 \pm 0.04	0.790 \pm 0.03	0.599 \pm 0.07	0.401 \pm 0.10	10.088 \pm 1.56	0.824 \pm 0.09	0.439 \pm 0.42
Sub02	Nishimoto[28]	0.682 \pm 0.04	—	—	0.443 \pm 0.09	9.553 \pm 1.53	0.676 \pm 0.13	—
	Ours	0.734 \pm 0.04	0.765 \pm 0.03	0.596 \pm 0.07	0.465 \pm 0.11	10.932 \pm 1.68	0.796 \pm 0.12	0.425 \pm 0.43
Sub03	Nishimoto[28]	0.701 \pm 0.04	—	—	0.441 \pm 0.08	9.576 \pm 1.74	0.682 \pm 0.16	—
	Ours	0.679 \pm 0.04	0.794 \pm 0.03	0.591 \pm 0.07	0.466 \pm 0.12	11.089 \pm 1.65	0.863 \pm 0.11	0.397 \pm 0.43
Sub04	Nishimoto[28]	0.702 \pm 0.04	—	—	0.446 \pm 0.09	9.537 \pm 1.61	0.665 \pm 0.16	—
	Ours	0.673 \pm 0.04	0.810 \pm 0.03	0.587 \pm 0.07	0.479 \pm 0.13	11.410 \pm 1.81	0.848 \pm 0.11	0.381 \pm 0.42
Sub05	Nishimoto[28]	0.676 \pm 0.04	—	—	0.442 \pm 0.08	9.498 \pm 1.39	0.650 \pm 0.14	—
	Ours	0.689 \pm 0.04	0.810 \pm 0.03	0.592 \pm 0.07	0.458 \pm 0.12	10.814 \pm 1.60	0.807 \pm 0.12	0.406 \pm 0.44
Sub06	Nishimoto[28]	0.694 \pm 0.04	—	—	0.444 \pm 0.08	9.526 \pm 1.57	0.665 \pm 0.14	—
	Ours	0.709 \pm 0.04	0.783 \pm 0.03	0.597 \pm 0.06	0.489 \pm 0.13	11.337 \pm 1.70	0.834 \pm 0.12	0.446 \pm 0.43
Sub07	Nishimoto[28]	0.674 \pm 0.04	—	—	0.446 \pm 0.08	9.630 \pm 1.57	0.672 \pm 0.14	—
	Ours	0.681 \pm 0.04	0.802 \pm 0.03	0.578 \pm 0.07	0.458 \pm 0.11	10.889 \pm 1.58	0.857 \pm 0.11	0.329 \pm 0.42
Sub08	Nishimoto[28]	0.696 \pm 0.04	—	—	0.444 \pm 0.08	9.664 \pm 1.57	0.662 \pm 0.15	—
	Ours	0.709 \pm 0.04	0.802 \pm 0.03	0.592 \pm 0.07	0.467 \pm 0.13	10.893 \pm 1.56	0.820 \pm 0.13	0.376 \pm 0.43
Sub09	Nishimoto[28]	0.673 \pm 0.04	—	—	0.445 \pm 0.08	9.573 \pm 1.67	0.661 \pm 0.14	—
	Ours	0.731 \pm 0.04	0.788 \pm 0.03	0.594 \pm 0.06	0.502 \pm 0.12	11.310 \pm 1.57	0.820 \pm 0.12	0.400 \pm 0.42
Sub10	Nishimoto[28]	0.685 \pm 0.04	—	—	0.441 \pm 0.08	9.598 \pm 1.79	0.662 \pm 0.14	—
	Ours	0.684 \pm 0.04	0.777 \pm 0.03	0.590 \pm 0.07	0.465 \pm 0.13	11.128 \pm 1.91	0.858 \pm 0.12	0.408 \pm 0.43

Table 8: Quantitative comparison of reconstruction results on Algonauts2021 dataset.

E.4 A Detailed Ablation Study on Various Hyperparameters

	Semantic-level \uparrow		
	2-way-I	2-way-V	VIFI-score
$\alpha=0$ (w/o fMRI-T)	0.794 \pm 0.03	0.833 \pm 0.03	0.594 \pm 0.07
$\alpha=0.25$	0.792 \pm 0.03	0.823 \pm 0.03	0.593 \pm 0.08
$\alpha=0.5$ (Our Model)	0.809 \pm 0.03	0.837 \pm 0.02	0.602 \pm 0.07
$\alpha=0.75$	0.791 \pm 0.03	0.832 \pm 0.03	0.594 \pm 0.08
$\alpha=1.0$ (w/o fMRI-V)	0.787 \pm 0.03	0.812 \pm 0.03	0.584 \pm 0.08

Table 9: **Ablation study** on multimodal contrastive learning. Colors reflect statistical significance (paired t-test) compared to the Full Model. $p < 0.0001$ (purple); $p < 0.01$ (pink); $p < 0.05$ (yellow); $p > 0.05$ (green).

	Pixel-level \uparrow		
	SSIM	PSNR	Hue-pcc
Ratio=0	0.297 \pm 0.11	9.037 \pm 1.42	0.758 \pm 0.11
Ratio=0.2	0.276 \pm 0.11	8.847 \pm 1.59	0.767 \pm 0.12
Ratio=0.4	0.285 \pm 0.10	9.045 \pm 1.48	0.768 \pm 0.11
Ratio=0.6 (Our Model)	0.301 \pm 0.10	9.134 \pm 1.51	0.768 \pm 0.11
Ratio=0.8	0.296 \pm 0.12	9.057 \pm 1.60	0.767 \pm 0.12

Table 10: **Ablation study** on sparse causal mask ratio. Colors reflect statistical significance (paired t-test) compared to the Full Model. $p < 0.0001$ (purple); $p < 0.01$ (pink); $p < 0.05$ (yellow); $p > 0.05$ (green).

During the training of Semantic Decoder, we control the weighting of the contrastive learning loss between fMRI-text ($L_{BiInfoNCE}(f, t)$) and fMRI-video ($L_{BiInfoNCE}(f, v)$) through the hyperparameter α . We set different values for α (0, 0.25, 0.5, 0.75, 1.0), where $\alpha=0$ signifies the exclusion of $L_{BiInfoNCE}(f, t)$, and $\alpha=1$ signifies the exclusion of $L_{BiInfoNCE}(f, v)$.

Table 9 indicates that despite achieving optimal results for the three semantic-level metrics when α is set to 0.5, variations in α do not significantly affect the results, except when α is 1, suggesting that the contrastive learning loss of fMRI-video predominates. This finding aligns with the experimental results of Lin et al [16]. We attribute this phenomenon to two primary reasons: (1) The text labels are generated by the BLIP2 model, which is not a video captioning model and may suffer from "hallucination" issues, thus the labels do not perfectly reflect the video content. For instance, manual inspection reveals that the model would repetitively output "There are 1,2,3,4,5,6,7,8,9,1,2,3,4,5..." when describing a manual telephone. (2) Research by Zhang et al. [76] has shown that the effective marked length of the text branch in CLIP is relatively short, which limits its ability to process detailed descriptions.

Based on the experimental results of Tong et al.[52], there is significant visual information redundancy in videos that can be effectively harnessed by applying a considerable mask ratio (e.g., 0.9). We design a sparse causal mask within the Consistency Motion Generator, which randomly masks a portion of frame tokens at a certain ratio, ensuring that the model does not take shortcuts during training. It is important to note that since we have downsampled the video to 4Hz, applying a very large mask ratio may prevent the model from learning spatiotemporal information from coherent frames. We set multiple values for the mask ratio (0, 0.2, 0.4, 0.6, 0.8) and calculate the results on pixel-level metrics, as shown in Table 10. The results indicate that the choice of mask ratio does not significantly affect the hue of reconstructed videos, but when the ratio is set to 0.6, it is significantly optimal for the other two metrics.

E.5 Further Results on Interpretability Analysis

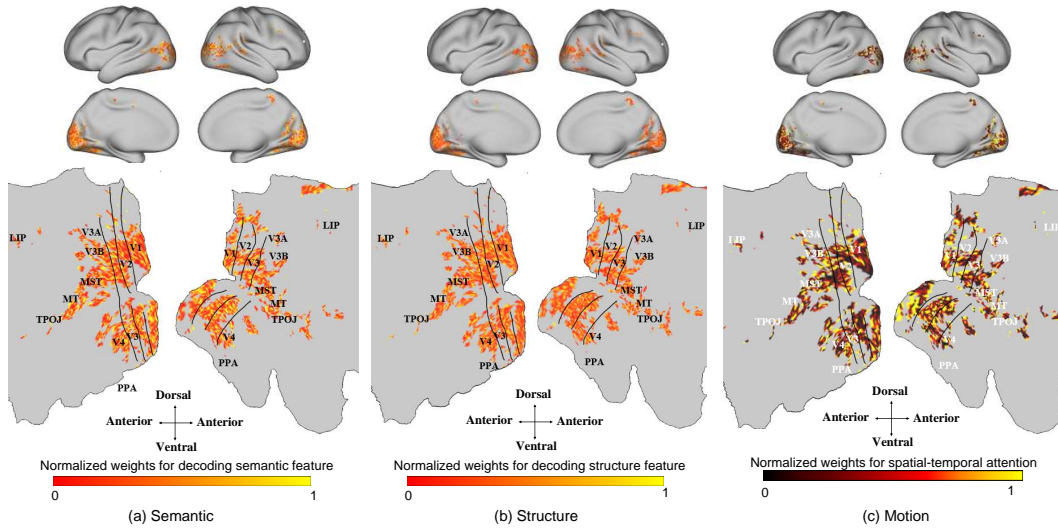


Figure 14: **Voxel-wise** importance maps projected onto the visual cortex of subject 2. The lighter the color, the greater the weight of the voxel in the interpretation of feature.

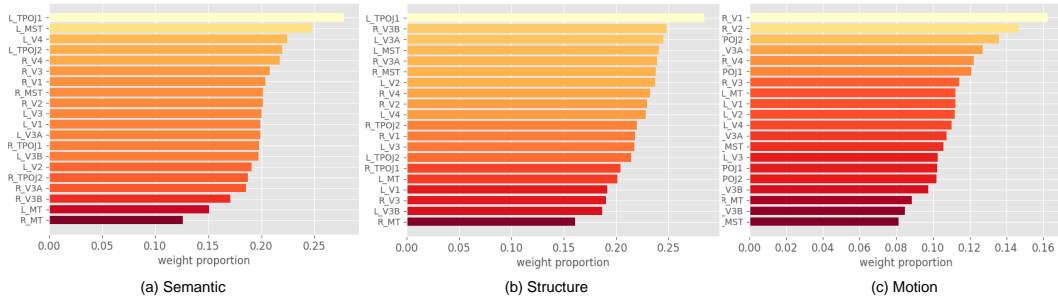


Figure 15: **ROI-wise** importance maps in the visual cortex of subject 2.

The visualization of voxel-wise and ROI-wise importance maps on Subject 2 and 3 is depicted in the aforementioned Figures.

F Limitations and Future Work

Our model, trained on data from a single subject, is not readily generalizable to other subjects and is markedly limited by the quantity of the training data. Going forward, we intend to create a multi-subject model for brain signal decoding and video reconstruction that effectively harnesses information from a diverse array of subjects and datasets.

